The Evolution of Asymmetries in the Tropical Cyclone Boundary Layer Wind Field during Landfall

JAMES HLYWIAK[a] AND DAVID S. NOLAN[a]

[a] *Rosenstiel School of Marine and Atmospheric Science, University of Miami, Miami, Florida*

(Manuscript received 19 July 2021, in final form 12 December 2021)

ABSTRACT: The evolution of the tropical cyclone boundary layer (TCBL) wind field before landfall is examined in this study. As noted in previous studies, a typical TCBL wind structure over the ocean features a supergradient boundary layer jet to the left of motion and Earth-relative maximum winds to the right. However, the detailed response of the wind field to frictional convergence at the coastline is less well known. Here, idealized numerical simulations reveal an increase in the offshore radial and vertical velocities beginning once the TC is roughly 200 km offshore. This increase in the radial velocity is attributed to the sudden decrease in frictional stress once the highly agradient flow crosses the offshore coastline. Enhanced advection of angular momentum by the secondary circulation forces a strengthening of the supergradient jet near the top of the TCBL. Sensitivity experiments reveal that the coastal roughness discontinuity dominates the friction asymmetry due to motion. Additionally, increasing the inland roughness through increasing the aerodynamic roughness length enhances the observed asymmetries. Last, a brief analysis of in situ surface wind data collected during the landfall of three Gulf of Mexico hurricanes is provided and compared to the idealized simulations. Despite the limited in situ data, the observations generally support the simulations. The results here imply that assumptions about the TCBL wind field based on observations from over horizontally homogeneous surface types—which have been well documented by previous studies—are inappropriate for use near strong frictional heterogeneity.

KEYWORDS: Coastal flows; Boundary layer; Hurricanes/typhoons; Buoy observations; Numerical analysis/modeling

1. Introduction

Surface friction–induced asymmetries in the tropical cyclone (TC) boundary layer (TCBL) wind structure over the ocean result from the translation of the TC. The constructive interference of the translation and cyclonic flow vectors results in boosted winds to the right (left) of motion in the Northern (Southern) Hemisphere, resulting in a cross-track gradient in the surface wind stress. Thus, while maximum Earth-relative winds typically reside to the right of motion (Klotz and Jiang 2017), enhanced radial convergence ahead of the TC accelerates TC-relative winds within the front-left quadrant (Shapiro 1983; Kepert and Wang 2001). Vertical wind shear modifies this structure independently of TC motion; increasing shear shifts Earth-relative maximum winds from downshear to left of shear, while increasing TC motion shifts the maximum toward the rear and right of motion (left of motion in the Southern Hemisphere). As a result, the maximum Earth-relative winds within a TC experiencing opposing motion and shear vectors usually occur to the right of motion, concomitant with maximum inflow downshear and to the right of motion (Zhang and Uhlhorn 2012; Zhang et al. 2013; Uhlhorn et al. 2014).

For a TC within coastal waters, the surface frictional field is marked by not only the translation effect but also by the presence of land. Unfortunately, little is known about how the structure of the TCBL wind field changes during landfall, outside of rapid weakening for winds crossing the coastline. Previous studies have provided evidence for the increased occurrence of transient features such as mesovortices and horizontal boundary layer roll vortices near land (Blackwell 2000; Morrison et al. 2005; Alford et al. 2019; Li et al. 2021). Well ahead of landfall, other studies of idealized numerical simulations of TC have suggested that bands characterized by high potential vorticity and low equivalent potential temperature wrap around the offshore side of a TC. Entrainment of these bands may then perturb the inner eyewall, forcing eyewall replacement-like cycles as the vortex symmetrizes (Chen and Yau 2003; Williams 2019).

Observations and numerical simulations of Hurricanes Frederic (1979), Mitch (1998), and Wilma (2005) suggest that the presence of land upstream forces the growth of higher-order wavenumber patterns to the TC inflow. Nolan et al. (2021a,b) showed that two wind analysis products that rely on observations from over the ocean—HWind (Powell et al. 1998) and the Tropical Cyclone Surface Wind Analysis (TCSWA) (Knaff et al. 2015)—broadly captured the surface total wind fields of Wilma near land compared to numerical simulations. However, these products disagreed with the simulated inflow over land. An analysis of the TCBL structure over the coastal waters was not the focus of these studies; however, Fig. 8 of Nolan et al. (2021b) reveals that inflow angles within the offshore flow of the numerical simulations increased significantly just before landfall. For the cases of Frederic and Mitch, strong inflow developed along the onshore coastline and to the left of motion before landfall, respectively (Powell 1982; Kepert 2006). Consequently, inflow angles greatly exceeded what is typically observed over the ocean. Additionally, Alford et al. (2020) compared radar and dropsonde data along the North Carolina coastline sampled during the landfall of Hurricane Irene (2011) to study the transition of the TCBL during across the coast. They note that the formation of the inland internal boundary layer (IBL) mixes an

---

Corresponding author: James Hlywiak, jhlywiak@rsmas.miami.edu

DOI: 10.1175/MWR-D-21-0191.1

increasingly deeper layer of the original TCBL, leaving the flow above unaltered. Thus, the TCBL tangential wind maximum—which typically resides within the inflow layer over the open ocean—is elevated above the TCBL and may remain intact for several kilometers inland.

There is also support within previous idealized studies for significant changes to the TCBL wind field caused by frictional convergence during landfall. Tang and Tan (2006), Wong and Chan (2007), and Szeto and Chan (2010) determined that the offshore flow was highly subgradient over the ocean, leading to enhanced inflow and subsequent upper-TCBL convergence. Similarly, Li et al. (2014, 2015) found greater vertical velocities and rainfall maxima within the offshore flow over water, a finding corroborated by observations within the South China Sea (Xu et al. 2014). Finally, Hlywiak and Nolan (2021) studied the sensitivity of the inland decay of the surface winds after landfall over a variety of inland surface characteristics using idealized simulations. In those simulations, frictional convergence before landfall accelerated a secondary circulation throughout the TCBL which was enhanced for increasing the surface roughness. This occurred first within the forward quadrants relative to the TC motion, suggesting that the response to the presence of land for a translating TC is highly asymmetric.

However, there is little observational evidence elsewhere in support of or contrasting the role of land in forcing enhanced offshore inflow, and the physical processes behind this evolution are not clear. Additionally, questions remain regarding subsequent effects on the total winds throughout the TCBL, including changes to the location and strength of supergradient TCBL jets. Here, we address these gaps in the literature through analysis of the evolution of the TC boundary layer wind field before and during landfall using idealized, mesoscale simulations. Specifically, we identify how the presence of land ahead of a landfalling TC affects the radial velocity field and the subsequent impacts on the total wind field. Additional sensitivity experiments include modifying translation speed and inland aerodynamic roughness length. Last, a brief analysis of observations of surface winds collected by coastal stations and offshore buoys during the landfalls of three Gulf of Mexico hurricanes is presented.

2. Methodology

a. Numerical methods

Simulations were performed using the Advanced Weather Research and Forecasting (WRF-ARW) Model, version 4.2.1. The experimental procedure was very similar to that of Hlywiak and Nolan (2021). First, an ocean-only case was performed, which will be referred to as OCN. Initialization consisted of embedding a weak vortex within the surrounding atmospheric environment following the point-downscaling method of Nolan (2011). Easterly winds below 850 hPa were 5 m s^{-1} and sinusoidally decreased to 2.5 m s^{-1} above 200 hPa, resulting in 2.5 m s^{-1} of westerly bulk vertical wind shear. Although not the focus of this study, background vertical wind shear was desired here to improve the realism of the simulations; all TCs in nature experience shear to some degree. Thus, including shear here resulted in a familiar and typical TCBL wind field over the ocean. Regardless, the vertical wind shear was light and had little to no impact on the inner core structure, and forced only a slight preference for higher inflow angles downshear. Translation speed was a fairly consistent 4.25 m s^{-1}. Motion can be approximated as due westward, which is accurate to within 10° throughout the duration of each simulation. Sea surface temperatures remained static in time and in space at 27°C, to simplify the thermal discontinuity at the coastline. The mean tropical sounding of Jordan (1958) was used to initialize the atmospheric temperature and moisture vertical profiles. OCN was integrated forward in time over eight days. Landfall simulations were initialized from OCN at the start of the fifth day and were integrated over four additional days, making landfall roughly three days after restarting. Simulations were performed within a large outer parent domain of horizontal resolutions $\delta x, y = 27$ km on an f plane equivalent to the Coriolis parameter at 20°N. Three nested, vortex-following domains facilitated finer resolution of the inner core. These domains featured resolutions of $\delta x, y = 9$, 3, and 1 km. Nudging of the environmental sounding toward the initial state was applied to the outermost domain only using the time-varying PDS (TVPDS) method of Onderlinde and Nolan (2017) with a nudging time scale of $\tau = 12$ h. Nudging was enabled in order to minimize modifications to the TC structure unrelated to the change in surface conditions. 51 vertical levels were enabled using the stretched WRF pressure coordinate system, with 19 of these levels concentrated below roughly 2 km. Wind and pressure variables at each height were saved every 2 min, while other variables were saved every 10 min.

The Mellor–Yamada–Janjić (MYJ) planetary boundary layer scheme was enabled for all simulations (Janjić 2002). The version of MYJ used here differs from the standard package provided by WRF in two ways. First, the drag coefficient over water was updated to match Edson et al. (2013), for which the drag coefficient saturates at high wind speeds. This relationship has been thoroughly verified by previous studies (Donelan et al. 2004; Bell et al. 2012; Green and Zhang 2013). Enthalpy fluxes were computed using a constant moisture roughness length (isftcflx = 1 within WRF). Second, a line of code originally commented out in the WRF MYJ module was reinstated to increase the sensitivity of the 10 m winds to the aerodynamic roughness length following the advice of the authors of Cao and Fovell (2016). Offline tests as well as results from that study and Nolan et al. (2021a,b) reveal a significant improvement in the computed diagnostic 10-m wind field when using this modification. Additional experiments for this study using the Yonsei University (YSU) PBL scheme (Hong et al. 2006) produced TCs featuring stronger maximum winds (5 m s^{-1}) and deeper minimum pressures (5 hPa); however, the overall TCBL structure, depth, and evolution throughout the simulation revealed similar results (not shown). Readers are encouraged to refer to Nolan et al. (2009a,b, 2021a,b) for discussions on the differences in overall PBL characteristics between solutions of MYJ and YSU within WRF. The WRF single-moment 5 (Lim and Hong 2005) microphysics option was enabled, and convection was parameterized for the outermost domain using the modified Tiedtke scheme (C. Zhang et al. 2011). Incoming solar and outgoing longwave radiation schemes were disabled to remove the effects of the diurnal cycle.

The Noah land surface model (Chen and Dudhia 2001) was used to parameterize surface fluxes, where the soil is specified as having loam characteristics. The majority of the following landfall analysis reflects a single, control simulation. The inland aerodynamic roughness length Z_0 used for the control simulation was 25 cm, thus this simulation will be referred to as Z25. The volumetric soil moisture content S_c was set to 0.30 and remained static in time. Additional simulations consisting of a fast background steering flow with identical surface characteristics to Z25 as well as inland Z_0 values of 5 and 50 cm are discussed in sections 4a and b. The land surface temperature is held constant to remove alterations to the TCBL associated with changes in heat fluxes at the coast, as this was not the focus of the research. For a more detailed analysis of how inland temperature changes affect the near-surface wind field, refer to Hlywiak and Nolan (2021).

b. The TCBL wind structure over the ocean

Figure 1 reveals the TC intensity by maximum 10-m total wind speed ($S10_{\mathrm{max}}$), minimum surface pressure (P_{min}), and the azimuthally averaged maximum tangential winds at 10 m and 2 km (V_t10_{max} and $V_t2\mathrm{km}_{\mathrm{max}}$) for OCN and Z25. Both TCs experienced a similar intensity evolution by all three metrics and plateaued above 65 m s^{-1} for two full days before landfall. Z25 decayed rapidly upon landfall. Intensity changed very little over the two days before landfall, besides slight intensification over the 24 h before landfall. The P_{min}, V_t10_{max}, and $V_t2\mathrm{km}_{\mathrm{max}}$ of Z25 weakened roughly 5 h before landfall; however, the $S10_{\mathrm{max}}$ of Z25 briefly increased by more than 5 m s^{-1} at 2 h before landfall. This spike in intensity before landfall was related to the formation of mesoscale eyewall vortices (not shown).

Figures 2 and 3 show the azimuthal-mean tangential and radial winds—V_t and V_r— below 3 km for OCN at $t = 170$ h. Each field is averaged within the four TC motion-relative quadrants. Also plotted are the height of the maximum V_t, the depth of the inflow layer—defined as the height at which the radial velocity exceeds 10% of the quadrant-averaged minimum in radial velocity as in J. A. Zhang et al. (2011a)—and the TCBL height computed by the MYJ scheme. The latter is essentially the height at which the turbulent kinetic energy (TKE) falls below a threshold. This threshold value is a function of the master mixing length, which changes based on the stability and shear production within the layer (Janjić 2002).

The weak yet persistent environmental shear acting on the TC plus the steady westward motion forces slight asymmetries within the TCBL. The overall structure is in good agreement with analysis of dropsonde composites within mature TCs (J. A. Zhang et al. 2011b, 2013). The region of highest V_t near the RMW was fairly symmetric and was centered between heights of 500–700 m. The V_r near the surface was most intense within the front-right quadrant due to the translation effect; however, the inflow layer was much deeper behind the TC as a result of the slight vortex tilt due to the wind shear. The inflow layer mirrors the TCBL depth defined by the TKE, revealing an increase in depth with increasing radius out to roughly 2–3 times the RMW followed by a steady decrease with increasing radius. The inflow depth was shallower within the front quadrants and deeper within the rear quadrants—which also align with the upshear and downshear quadrants—which is in agreement with the composite profiles revealed in Zhang et al. (2013). Of the three definitions, the TKE-based TCBL depth has the sharpest peak near the RMW where the vertical wind shear and TKE production is greatest, yet follows a similar decrease with increasing radius at large radii. Thus, despite the slight differences between the depth of the TCBL provided by each unique definition, when considering the above evidence, it is clear that three km is an appropriate upper bound for the following analysis of the TCBL.

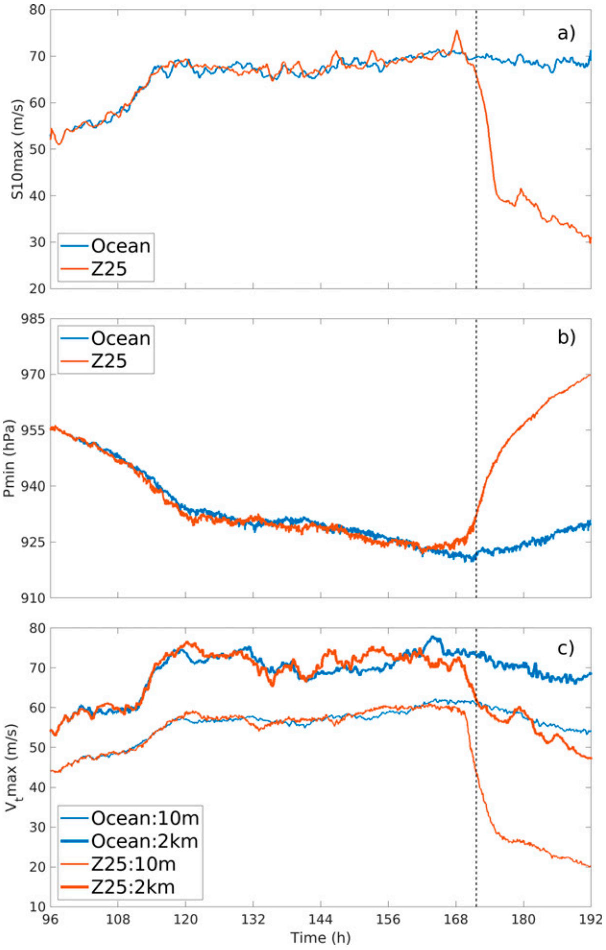

FIG. 1. (a) Maximum 10-m wind speed (m s^{-1}), (b) minimum central pressure (hPa), and (c) maximum azimuthal-mean tangential wind speed at 10 m (thin plots) and 2 km (thick plots) (m s^{-1}) for OCN (blue plots) and Z25 (red plots) cases.

3. Evolution of the near-surface winds during landfall

a. Development of enhanced inflow within the offshore flow

The sudden decay in intensity shown in Fig. 1 masked the more complex evolution of the near surface flow, beginning

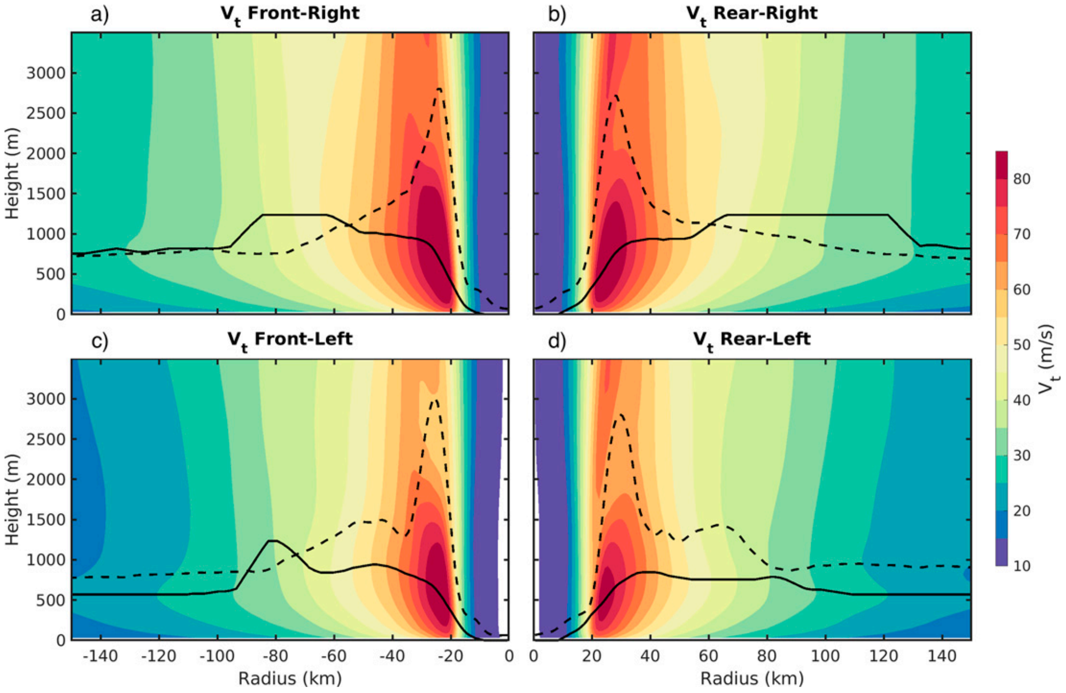

FIG. 2. Azimuthally averaged tangential winds V_t by quadrant for OCN at $t = 170$h. The height of the maximum V_t is plotted as the solid black line while the TCBL height determined by the MYJ scheme based on the TKE field is shown in the dashed black line.

several hours before landfall. Figure 4 reveals Hovmöller diagrams of Earth-relative V_t and V_r at the lowest model level for Z25 as a function of azimuth relative to the TC center at each analysis time, averaged within a radial band extending from the RMW to 20 km outside of the RMW. Periodic, cyclonically traveling streaks in both V_t and V_r maxima associated with mesovortices were ubiquitous features well before landfall. Streaks of inflow maxima generally originated to the

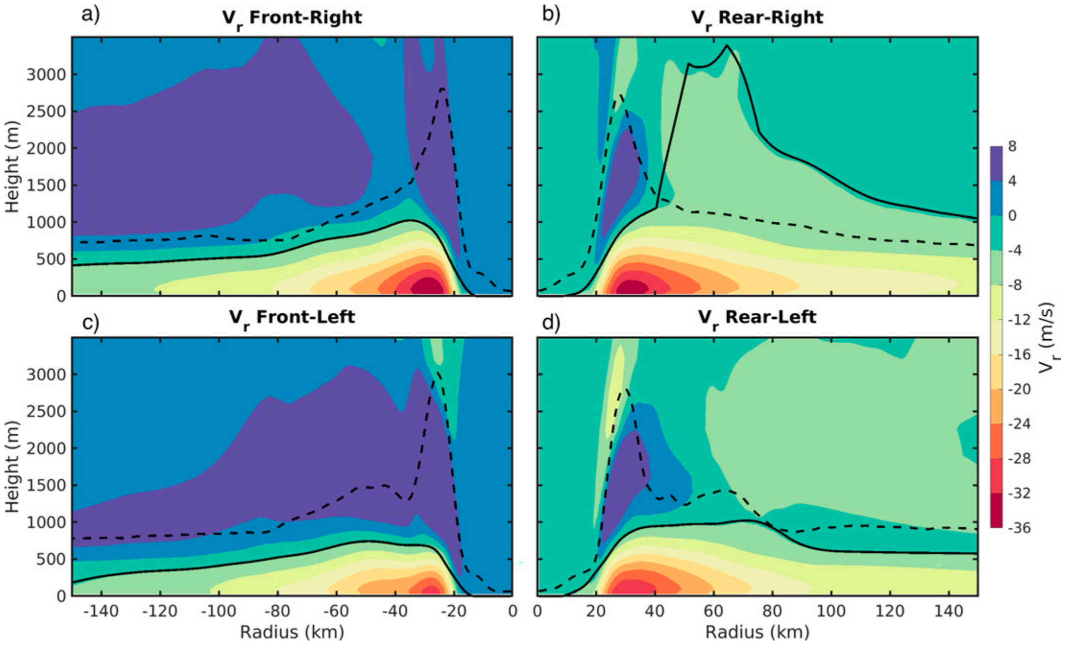

FIG. 3. As in Fig. 2, but for the azimuthally averaged radial winds V_r by quadrant for OCN at $t = 170$ h. The depth of the inflow layer as defined in the text plotted as the solid black line while the TCBL height determined by the MYJ scheme based on the TKE field is shown in the dashed black line.

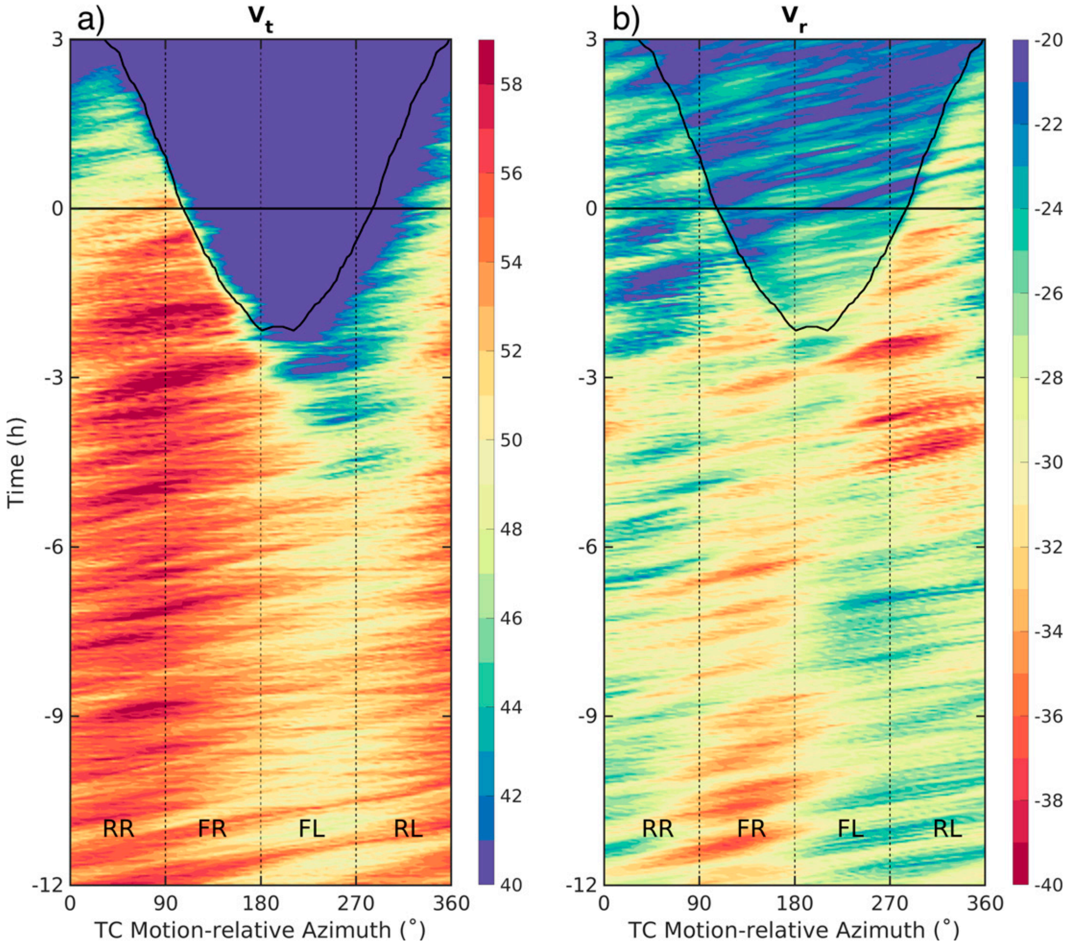

FIG. 4. Azimuthal–time Hovmöller diagram of (a) tangential and (b) radial winds (m s^{-1}) at the lowest model level, averaged within a radial band from the RMW to 20 km outside of the RMW as a function of TC-motion relative azimuth, wrapping cyclonically around the TC. The horizontal black lines at $t = 0$ indicate the time of landfall, while the black plot that varies in time indicates the moment at which that portion of the flow reached land, approximated using the center of the radial annulus.

right of motion and accelerated within the front-right quadrant. Maxima in V_t originated within the rear-left quadrant and propagated through the right quadrants before decaying in the front-left quadrant.

Figure 4b shows that from 9 to 6 h before landfall, the radial velocity within the front-right quadrant decelerated. Conversely, beginning 6 h before landfall, the inflow within the rear-left quadrant rapidly accelerated. As the TC approached land, this inflow maximum rotated anticyclonically toward the front left and increased in magnitude. At the same time, the inflow within the front-right and rear-right quadrants continued to weaken, despite this quadrant being characterized by onshore flow. During this time, Fig. 4a reveals that the downstream V_t within the right quadrants accelerated. Strong winds persisted right up to the point at which the flow reached the shoreline. Meanwhile, V_t within the region of enhanced inflow weakened, and a band of weak V_t occurred along the offshore coastline. The effect of the changes in V_r on the total winds is discussed in section 3b.

Figure 5 offers a top-down view of Z25 at $t = -15$ and -3 h before landfall, showing the vertically averaged gradient wind ratio—defined as the vertically averaged ratio of V_t to the gradient wind V_{gr}—below 1 km as well as the inflow angle at $z = 250$ m. At $t = -15$ h, supergradient flow was collocated with the RMW, forming a symmetric band. Outer streaks of supergradient flow coinciding with spiral rainbands were mostly found to the right of motion. The majority of the flow to the left was subgradient. Inflow angles for most of the period over the ocean were strongest ahead of the TC at small radii, rotating anticyclonically with increasing radius and maximizing between 25° and 30°.

By $t = -3$ h, the vertical layer below 1 km became increasingly more subgradient with distance downstream over land. The subgradient part of the flow was collocated with large inflow angles in excess of 45° out to a radius of 100 km. This is in stark contrast to the left-of-motion flow over the ocean, for which inflow was very weak. Thus, there appears to be a correlation between the increasing departure of the flow from gradient wind balance and

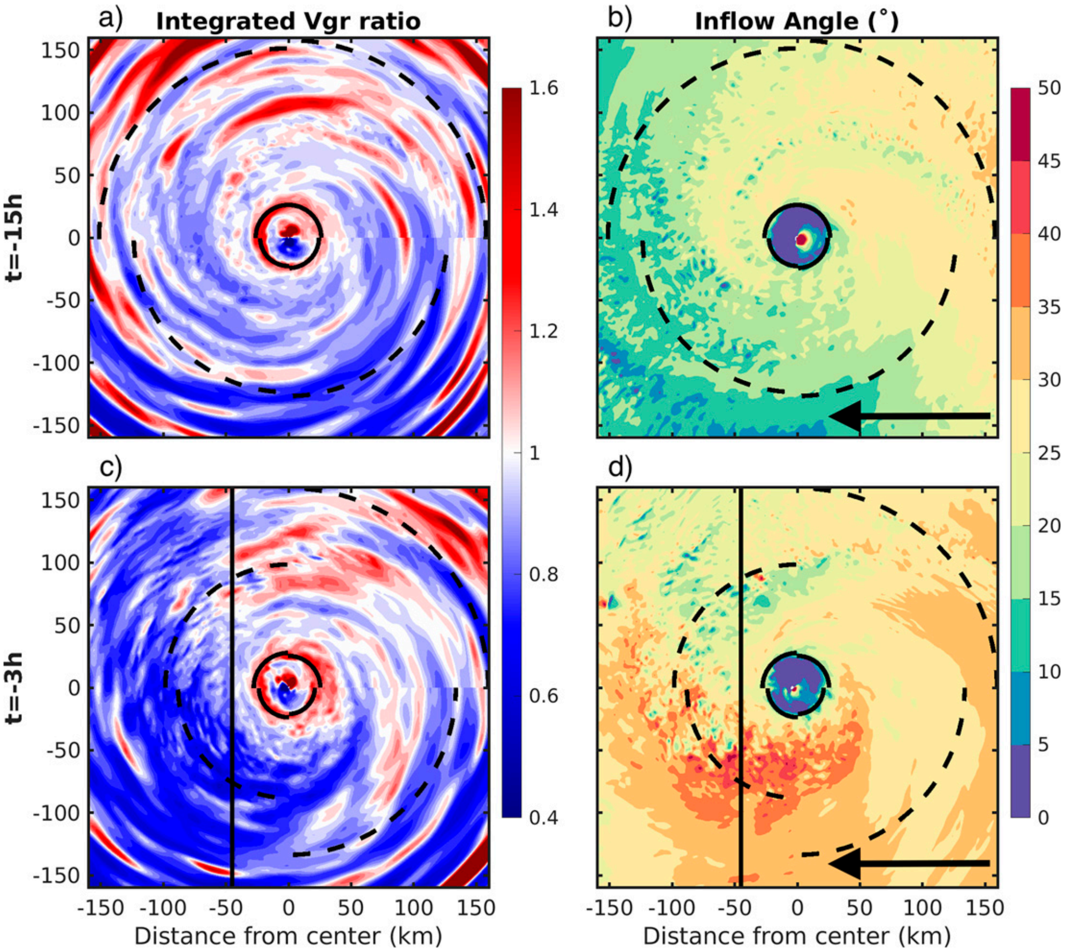

FIG. 5. (a),(c) Vertically averaged gradient wind ratio below $z = 1$ km. Less (greater) than 1 indicates the mean flow is sub- (super)-gradient. (b),(d) Inflow angle for Z25 at $z = 250$ m, where positive indicates inflow. Two times are shown: (top) 15 and (bottom) 3 h before landfall. The black solid (dashed) lines indicate the azimuthally averaged RMW (tropical force wind radius) by quadrant. The vertical black solid line indicates the position of the coastline. The black arrows in (b) and (d) indicate the direction of motion.

distance inland. Additionally, winds around the RMW became more supergradient, especially within the rear quadrants. This latter result is expounded in section 3b.

To determine the direct causes for the enhanced offshore inflow, Fig. 6 shows the individual contributions by the dominant forces represented in the V_r equation of motion at $t = -4$ h, vertically averaged below $z = 500$m. The approximated V_r budget is shown below as (1):

$$\frac{dV_r}{dt} = -\frac{1}{\rho}\frac{\partial p}{\partial r} + fV_t + \frac{V_t^2}{r} + F_r. \qquad (1)$$

The term on the left-hand side is the total derivative, and the terms on the right-hand side in order are the pressure gradient, Coriolis, centrifugal, and frictional terms. The frictional term here is computed by the PBL scheme in WRF. The pressure gradient, friction, and centrifugal terms dominated the V_r budget within 50 km of the center. Outside of this range, the centrifugal force weakened considerably. A local minimum in the frictional deceleration within the offshore flow over water coincided with very slight minima in the Coriolis and centrifugal forces, while the pressure gradient force remained relatively unaffected. The net effect is enhanced negative radial velocity—i.e., positive inflow—tendency within the front-left quadrant. Thus, the acceleration of the offshore inflow was driven by the weakening of the frictional deceleration, which occurred instantaneously in contrast to the slower relaxation of the highly agradient offshore flow back toward gradient wind balance.

b. Changes to the total wind field

The enhanced V_r within the offshore flow contributed to significant changes to the angular momentum field before landfall. Figure 7 shows the advective tendency of angular momentum by the radial and vertical winds M_{adv}, i.e., (2), vertically averaged between two layers—from the lowest model level to 1 km and between 1 and 3 km—as well as radially averaged between the RMW and 30 km outside the RMW:

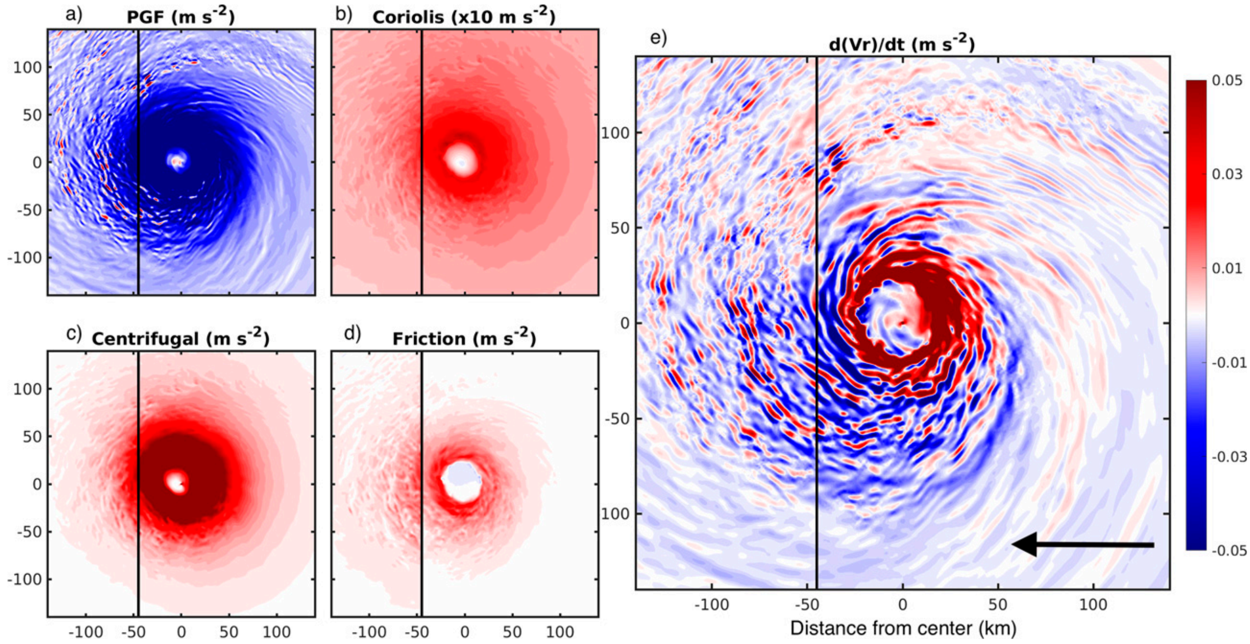

FIG. 6. (a)–(d) Pressure gradient, Coriolis, centrifugal, and Reynolds wind stress forces as in (1) (m s^{-2}) for Z25 at $t = -3$ h. Fields are vertically integrated and averaged below a height of 500 m. Note that the Coriolis force is multiplied by 10 in (b). (e) The total derivative of the radial velocity computed as the sum of the four terms on the right hand side of Eq. (1), where blue (negative) indicates inflow acceleration and red (positive) indicates outflow acceleration. As before, the black arrow in (e) indicates the direction of motion.

$$M_{\mathrm{adv}} = -\left(V_r \frac{\partial M}{\partial r} + w \frac{\partial M}{\partial z}\right). \tag{2}$$

In addition, regions of vertical velocity greater than 1 m s^{-1} at the top of each layer are also plotted. Beginning with the lower layer, M_{adv} was greatest within the front-right quadrant and slightly negative to the left well before landfall, coinciding with the inflow patterns from Fig. 4b. M_{adv} was greatest below 1 km and regulated more by the inflow field than the vertical velocity field within the lower layer. In fact, regions of strong vertical velocity were associated with weaker M_{adv} below 1 km. Beginning around $t = -5$ h, M_{adv} within the rear-left and right quadrants increased substantially within the lower layer. Additionally, the enhanced offshore inflow led to greater TCBL convergence offshore (not shown), which resulted in greater vertical velocities downstream within the rear quadrants and to the right of motion. As the front portion of the wind field crossed the coastline, M_{adv} remained strong within the rear-left and rear-right quadrants.

Within the layer between z = 1–3 km, M_{adv} was regulated more by the vertical advection as opposed to the radial advection. The M_{adv} within this annulus was weak well before landfall, but as convergence and vertical velocities increased to the rear and to the right, so did M_{adv}. While M_{adv} was greatest within the rear-left quadrant within the lower layer, the upper layer featured greatest M_{adv} roughly 90° downstream within the rear-right quadrant. Thus, it appears that the enhanced offshore inflow increased radial advection of positive angular momentum and radial convergence within the offshore flow near the surface. This enhanced angular momentum was then elevated vertically and advected downstream.

Consequently, changes to the M_{adv} field manifested as changes to the tangential winds near the top of the TCBL. Figure 8 shows azimuthal transects—also known as curtain plots—of the Z25 and OCN flows below 3 km averaged within a radial distance of r = 60–90 km from the center at $t = -2.5$ h and the corresponding time for OCN. Note that this annulus intersects where the mean V_{gr} ratio over land was most subgradient in Figs. 5c,d, and does not overlap with the annulus shown in Fig. 4. Beginning at 0°—due east—and traveling cyclonically with increasing azimuth, the OCN TCBL flow to the right of motion (0°–180°) featured moderate inflow below 1 km and strong V_t around an altitude of 2.5 km. Within the front quadrants of OCN—between 90° and 270°—outflow occurred above weak inflow which co-aligned with weaker V_t. The TCBL height defined by the TKE field decreased slightly within the front-right quadrant (90°–180°) before deepening to about 1.2 km within the front-left quadrant (180°–270°). This height changed little downstream. The flow to the left of the TC (180°–360°) was characterized by a V_t minimum aloft and a deepening of the inflow layer concomitant with a deep subgradient layer which stemmed from the surface.

The same transect for Z25 before landfall featured key differences. First, the upper-TCBL V_t within the right quadrants was stronger and more supergradient. This supergradient layer extended farther toward the surface than for OCN and intruded farther downstream over land. Additionally, inflow ahead of Z25—i.e., over land—accelerated with distance downstream

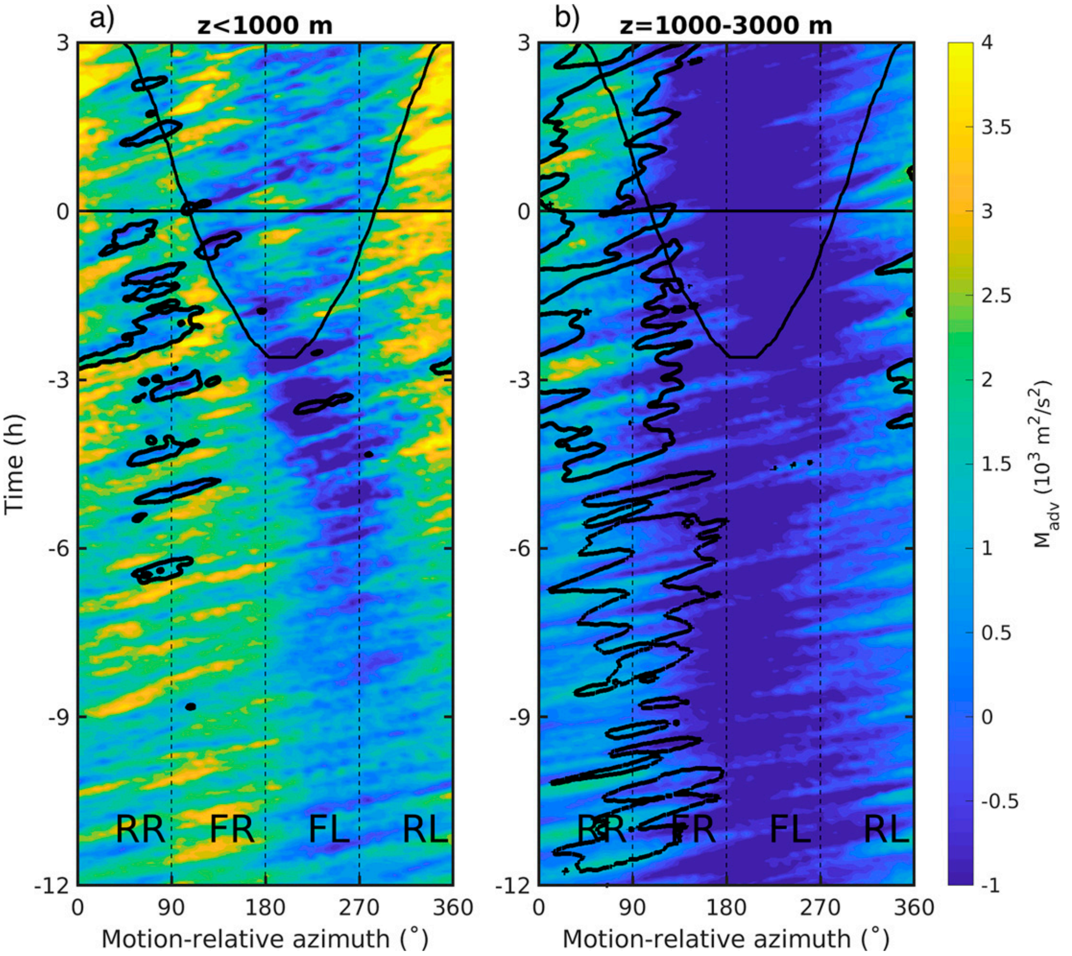

FIG. 7. As in Fig. 4, but for $M_{\rm adv}$ ($\times$ 10^3 $\rm m^2$ $\rm s^{-2}$); $M_{\rm adv}$ was averaged vertically within two layers: (a) below z = 1000 m and (b) between z = 1000–3000 m. Additionally, $M_{\rm adv}$ was radially averaged from the instantaneous azimuthal-mean RMW out to 30 km outside of the RMW. Vertical velocities in excess of 1 m $\rm s^{-1}$ within this annulus are contoured as well.

and coincided with an increasingly deeper subgradient layer, which further deviated from gradient wind balance with increasing azimuth, reaching a maximum depth—defined by values for which the ratio was equivalent to or less than 1—and minimum $V_{\rm gr}$ ratio within the front-left quadrant over land. At the same time, the outflow layer aloft over land was stronger than for OCN, reflecting an accelerated near-surface secondary circulation. The TCBL height continued to deepen over land, reaching a maximum of approximately 1.6 km directly over the offshore coastline. This increase in TCBL depth with distance inland is in agreement with radar observations within Hurricane Irene (2011) (Alford et al. 2020). Thus, the longer the flow was exposed to land, the deeper and more subgradient the TCBL became. The offshore TCBL over the ocean relaxed closer toward gradient balance, despite the acceleration of deep inflow. However, upper-TCBL winds downstream of the enhanced inflow accelerated relative to OCN. Additional examination of Fig. 5c reveals a wide supergradient region behind the TC, which provides further evidence of a stronger TCBL jet to the rear of the TC.

We now focus on the changes to the vertical profiles of wind just before landfall near the RMW. Figure 9 shows near-surface V_t, V_r, and $V_{\rm gr}$ at two times—8 and 3 h before landfall—averaged within a radial band of 30–50 km from the center at three TC-relative locations. These locations represent the immediate onshore flow (location A), offshore flow (location B), and upstream from the immediate onshore flow (location C). We note that during this time frame, the RMW remained between 20 and 25 km, yet the wind field of the TC expanded slightly. Regardless, the greatest changes to the wind field during this time were those forced by the coastline. The onshore (A) V_t below 200 m did not change significantly within this time, yet V_t increased above an altitude of 1 km. The $V_{\rm gr}$ increased throughout the profile; thus, the onshore flow beneath 300 m became slightly more subgradient despite little change to V_t below this level. At the same time, the winds above this were slightly more supergradient, in line with the deepening of supergradient winds revealed in Fig. 8e. Conversely, the onshore V_r profile near land changed little over the course of this time period. Thus, the spatial-

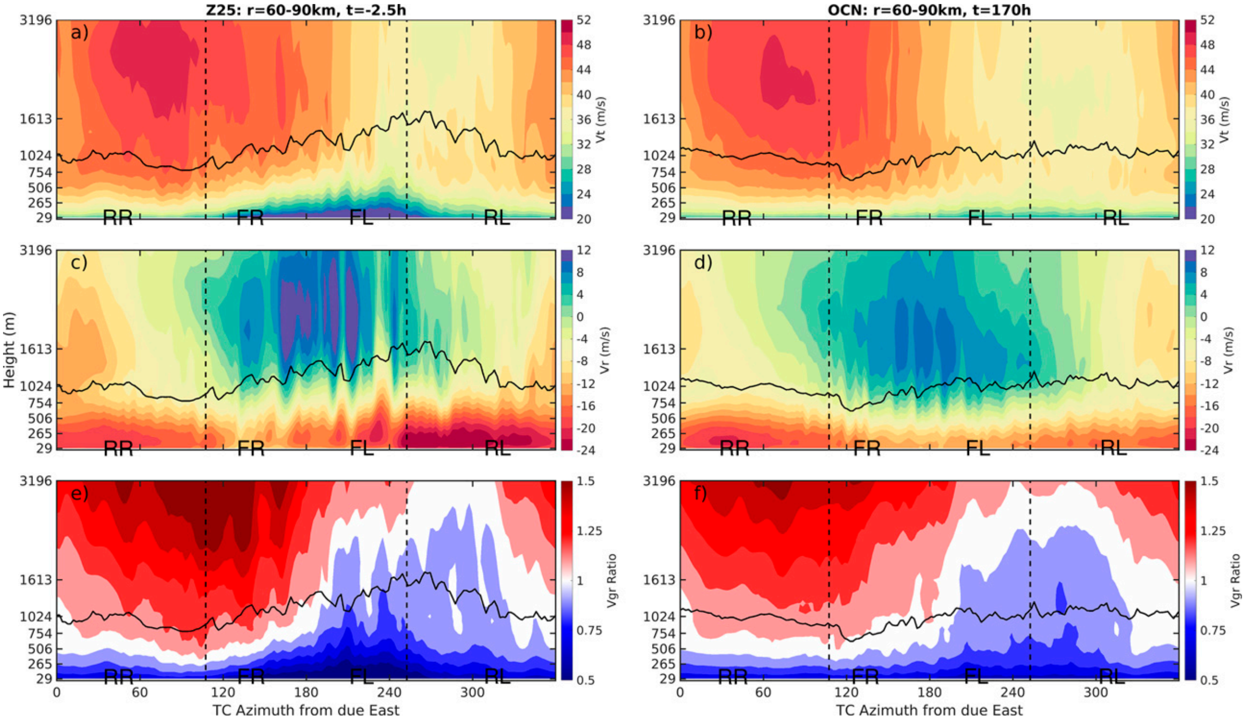

FIG. 8. (a),(b) V_t (m s^{-1}); (c),(d) V_r (m s^{-1}); and (e),(f) V_{gr} ratio (unitless) for (left) Z25 and (right) OCN as functions of TC azimuth, where 0° marks due east and increases cyclonically around the TC. Each panel features annotations at approximately 45°, 135°, 225°, and 315° corresponding to the rear-right, front-right, front-left, and rear-left quadrants. The time for the Z25 plots is $t = 2.5$ h before landfall and for the OCN plots is $t = 170$ h. The solid black line shows the depth of the TCBL defined from the TKE field. Each field is averaged within a radial band from $r = 60$–90 km from the center. The left and right vertical dashed lines indicate the onshore and offshore coastlines, respectively, and are also plotted for OCN for comparison.

mean onshore flow retained characteristics similar to that over the open ocean.

Within the offshore flow (B), the inflow layer near the surface deepened by roughly 200 m concomitant with an increase in the maximum inflow from 24 to 30 m s^{-1}. Similarly, the outflow layer aloft deepened by several hundreds of meters and increased in magnitude. Offshore V_t below 800 m decelerated substantially, and the flow below this level was highly subgradient, as previously observed. Additionally, the tangential flow above the subgradient layer became more supergradient and increased in magnitude above 2 km. Thus, the offshore flow retained characteristics of the upstream flow over land.

At location C, V_t above an altitude of 3 km increased. At the same time, the inflow layer was deeper than for over the open ocean while a weak outflow layer developed above 2 km. Therefore, changes to the winds in this region mainly occurred above the near-surface subgradient layer, as the upper-TCBL winds became more supergradient. Thus, the transition of the TCBL winds from location B back to A was characterized by the relaxation from a large deviation from gradient wind balance throughout the column toward a typical ocean vertical profile. The near-surface winds recovered faster, as the winds above an altitude of 500 m within the rear-right quadrant—and to a lesser extent, the front-right quadrant—were still marked by supergradient winds.

These modifications to the TCBL flow impacted the asymmetric RMW and the extent of strong winds at the surface. Figure 10 shows time series of the surface RMW and the total area encompassed by tropical storm force winds normalized by that of OCN and delineated by quadrant. These signals were periodic, and the timing of landfall for each quadrant differed. However, two key results stand out. First, the RMW within the quadrants to the left contracted by as much as 5% relative to OCN before landfall. This reflects the weak V_t near the RMW within the offshore flow. Conversely, the RMW within the right quadrants expanded by a few percent up until reaching land. Second, the area of tropical storm force winds expanded by 10%–15% to the left of the TC before reaching land. This was because although V_t was weaker immediately offshore, enhanced V_r contributed significantly to the total wind field. The quadrants to the right featured nearly equivalent extents of tropical storm force winds as for the ocean case.

Figure 11 compares spatial asymmetries in the total, tangential, and radial wind fields for Z25 with that of OCN just before landfall, providing a general summary of the patterns expounded above. Asymmetries here are represented by the sum of the wavenumber-1–5 components. It is important to note that the asymmetries were small compared to the symmetric mode; the asymmetries represented at most roughly 12% of the total wind field as opposed to roughly 85%

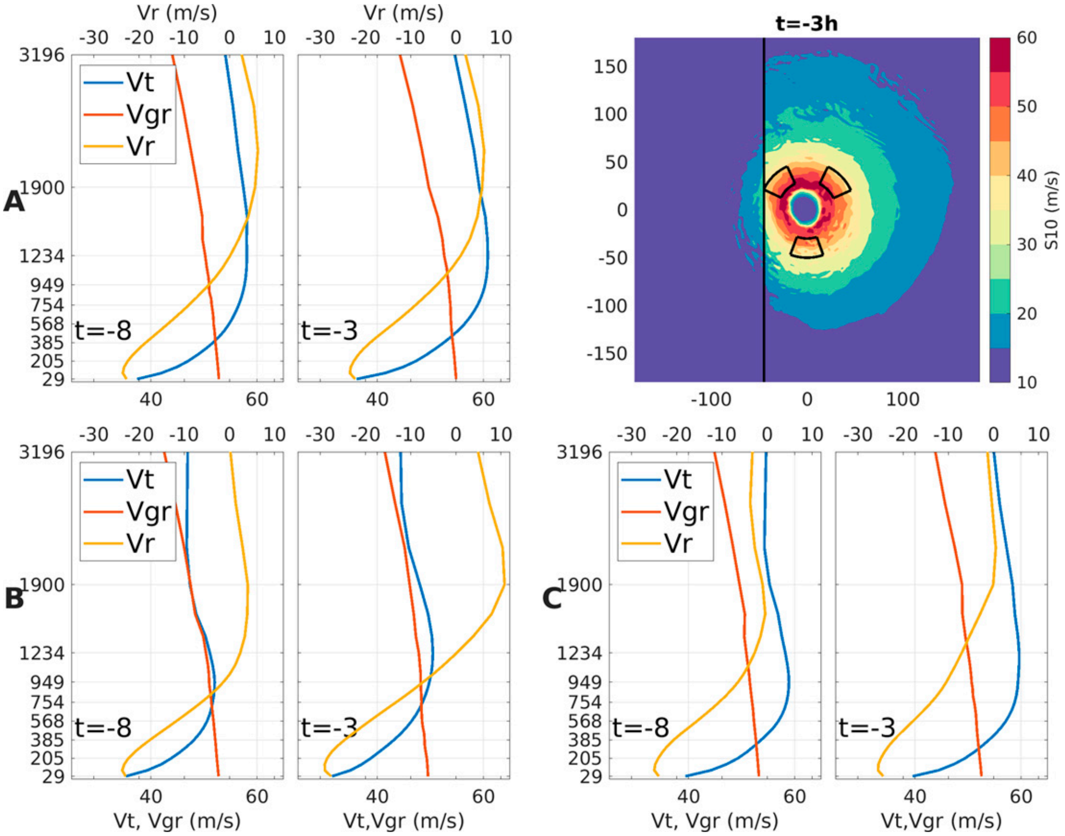

FIG. 9. Vertical profiles of V_t (m s^{-1}, blue), V_{gr} (m s^{-1}, red), and V_r (m s^{-1}, green), averaged within a radial band from r = 30–50 and an azimuthal band spanning 40° centered at 135° (location A), 270° (location B), and 45° (location C) counterclockwise from due east. Profiles for 8 and 3 h before landfall are shown. A schematic of the 10-m wind speed at $t = -3$ h is shown in the top right to place the size of each averaging area into context with the rest of the wind field.

characterized by the symmetric flow before landfall. Away from land, the wavenumber-1 mode was the dominant asymmetry for all three wind fields. The S10 and V_t10 were strongest within the front-right quadrant, slightly downstream from the inflow maximum.

Near land, asymmetries were dominated by weaker flow over land and stronger flow over the ocean. The higher-order asymmetries reveal more complex patterns in agreement with the preceding analysis. First, the maximum inflow—i.e., minimum radial velocity—asymmetry is clearly located to the left of the TC, reaching a peak between r = 40 and 80 km (Fig. 11c). Additionally, a positive anomaly in radial velocity occurs within the right-of-motion RMW, despite this region being associated with a negative anomaly for OCN case. The S10 and V_t anomalies within the onshore flow are characterized by positive anomalies. Offshore S10 anomalies near the RMW were slightly negative due to the reduction in V_t10, yet positive at larger radii as the enhanced inflow comprised a significant portion of the total wind field. Note that the negative anomaly in V_t10 over land is greater than the decrease of the inflow, especially within the front-left quadrant. Thus, even though the inflow decreases, the inflow *angle* increases (Fig. 5d). Although not shown here, the wavenumber-1 asymmetry dominated the flow at z = 2 km. Additionally, the influence of land was weak aloft compared to at the surface, as Z25 and OCN revealed similar asymmetries. Thus, it appears that most of the spatial asymmetries forced by land decayed with height up to 2 km.

To summarize these findings, the frictional forcing from the presence of land ahead of the TC enhanced and deepened the inflow layer within the offshore TC flow, which began roughly 7 h before landfall and approximately 200 km offshore. This asymmetry was frictionally driven, as the longer the circulation was exposed to the rougher surface and intense vertical mixing, the greater the deceleration of the near surface winds and deeper the affected layer were. Thus, the offshore flow stretching from over land to roughly 50 km out over the ocean was characterized by deep, strong inflow due to the relaxation in the centrifugal, Coriolis, and frictional forces concomitant with a relatively constant pressure gradient force. This deep inflow and subsequent radial convergence advected angular momentum above the TCBL and downstream, forcing an acceleration of V_t over water near the top of the TCBL. This result suggests that stronger wind gusts to the right of the TC

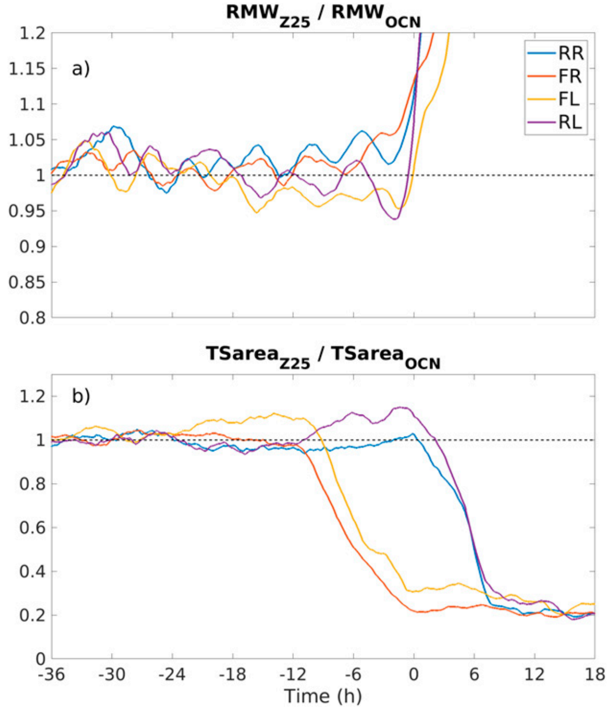

FIG. 10. (a) Time series of RMW and (b) area of tropical storm force winds by quadrant, normalized by the corresponding metrics for OCN. RR, FR, FL, and RL indicate the rear-right, front-right, front-left, and rear-left quadrants, respectively. Note that each quadrant reaches land at differing times, thus sudden changes to the rear quadrants lag the front by several hours.

near the coastline at the surface due to the presence of land are possible as the mean upper-TCBL tangential flow increases, assuming no change in the intensity of downward turbulent velocities. We note that the time-mean maximum tangential velocity for Z25 just before landfall is slightly weaker than for OCN, however (Fig. 11). A detailed analysis of gust factors requires saving data at a higher frequency than we have done here (2 min), to avoid aliasing highly energetic turbulent eddies. We save this for future work.

4. Sensitivity analyses

a. Translation speed

An additional simulation was performed to contrast the above results with a fast-moving TC. This simulation was initialized from OCN at the start of the fifth day, as for the previous simulations. For this simulation, TVPDS was used to nudge the background easterly winds from 5 and 2.5 m s^{-1} below 850 hPa and above 200 hPa to 10 and 7.5 m s^{-1} over the first day after initialization. Thus, the bulk vertical shear was the same as before, although the steering flow was increased. This simulation is referred to as Z25FAST.

Figure 12c reveals the increase in translation speed for Z25FAST occurred mainly within the first day after initialization and peaked 36 h after initialization. Z25FAST makes landfall with a translation speed around 7.5 m s^{-1}, compared to 4 m s^{-1} for Z25. The S10$_{\max}$ and $P_{\min}$ are shown in Figs. 12a and 12b. Z25FAST was marginally weaker than Z25, otherwise the intensity evolution was nearly identical. As with the control simulation, S10$_{\max}$ of Z25FAST increased by about 5 m s^{-1} a few hours before landfall despite a reduction in $P_{\min}$.

Figure 13 shows Earth-relative S10, V_t10, and V_r10 asymmetries for Z25 versus Z25FAST as in Fig. 11 at $t = -16$ h, before either TC experienced the effects of land. Increasing the translation speed amplified the wavenumber-1 pattern, which also rotated cyclonically by 45°–90°. Figure 14 shows the same asymmetric wind fields for when both TCs resided roughly 50 km offshore. The S10 and V_t10 negative anomalies over land and within the offshore flow were similar in areal extent and in magnitude between the two TCs. However, the positive anomalies in these fields to the right (within the onshore flow) were very similar to that for each TC several hours before. This provides further evidence that the onshore flow shares characteristics very similar to that over the open ocean, even when near land. Both simulations also featured a maximum in S10 within the right-rear quadrant (Figs. 14d,h).

Additionally, the right to left V_r10 asymmetry was amplified in Z25FAST. This is possibly due to the fact that the inflow maximum over the ocean for Z25FAST was located farther downstream cyclonically than for Z25. Thus, the asymmetries produced by land and the fast motion may constructively interfere. Still, the asymmetries forced by land are similar between these TCs. Finally, although not shown here, increasing the translation speed did little to affect the asymmetric field at 2 km outside a slight amplification of the along-coast gradient.

b. Surface aerodynamic roughness length

Two simulations featuring differing surface roughness values over land of $Z_0 = 5$ and 50 cm were performed using the same methods as for Z25. These simulations are referred to as Z05 and Z50. The intensities of both TCs were similar to each other for the majority of the simulation time period, as seen in Figs. 12a,b. Over land, Z50 decayed at a faster rate than Z05 and Z25. Differences in the values of $P_{\min}$ began 14 h before landfall, when the $P_{\min}$ of Z50 increased while Z05 briefly deepened. Conversely, the S10$_{\max}$ of Z05 follows nearly an identical progression to that of OCN up until landfall, while the S10$_{\max}$ of Z50 *increased* by several meters per second in the hours before landfall, despite the weakening in $P_{\min}$ of Z50. Further analysis revealed that the elevated S10$_{\max}$ before landfall was associated with mesovortices (not shown), as for Z25. However, it is interesting that this spike in S10$_{\max}$ was greater and lasted longer for increasing roughness. Analysis of the relationship between surface roughness and mesovortex activity before landfall is left for a future study.

Figure 15 reveals the inflow angle field at $z = 250$ m at $t = -10$, -6, and -2 h between Z05 and Z50. It is clear that increasing the Z_0 resulted in a greater enhancement of inflow angles within the offshore region, both in extent and in magnitude. Thus, inland roughness positively correlates with the

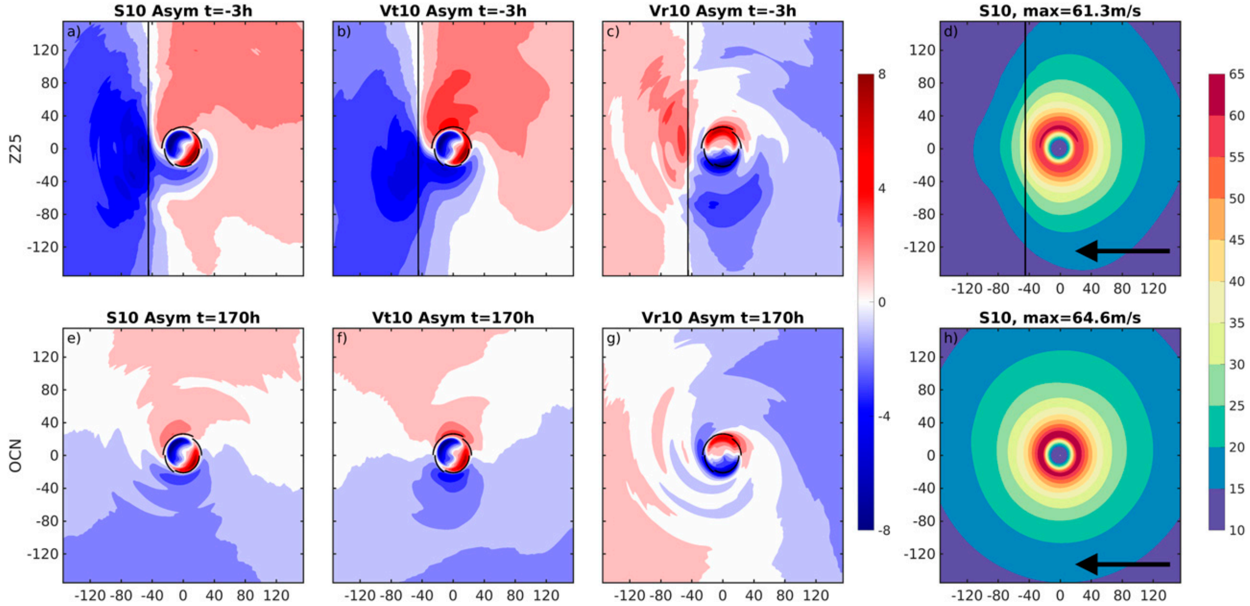

FIG. 11. Sum of wavenumber-1–5 modes of (a),(e) $S10$; (b),(f) V_t10; and (c),(g) V_r10 for (a)–(c) Z25 and (e)–(g) OCN averaged within a 1-h window centered at $t = -3$ h (equivalent to $t = 168$ h for OCN). (d),(h) The sum of the S10 wavenumber-0–5 components for Z25 and OCN, respectively. All fields are in m s^{-1}. The vertical black line marks the location of land for Z25. The S10$_{\max}$ for each TC is displayed in (d) and (h). The black arcs near the RMW in each plot note the RMW for six azimuthally averaged sectors of equal azimuthal width (60°). As before, the black arrows in (d) and (h) indicate the direction of motion.

amplitude of the inflow angle response of the TCBL to land revealed in section 3.

In Hlywiak and Nolan (2021), the enhancement of the angular momentum import by the radial velocity with increasing aerodynamic roughness length was discussed for a set of simulations similar to those performed in this study. In that study, this pathway led to increased winds within the original RMW during landfall for increasing roughness length, as well as a more marked outflow near a height of 3 km [see Fig. 11 of Hlywiak and Nolan (2021)]. We evaluate the azimuthal-mean response here as well, to compare with those previous results. Figure 16 shows the secondary circulation wind strength—i.e., $\sqrt{V_r^2 + W^2}$—and the V_t field for Z05 and Z50 at landfall, azimuthally averaged within the front quadrants over land (Figs. 16a–f) and the rear quadrants over the ocean (Figs. 16g–l). Within the front quadrants, the secondary circulation was dominated by strong inflow at the surface and outflow at a height of 1 km near the RMW which increased in height with increasing radius. The TC-wide maximum V_t and inflow were greater for Z05. However, the difference plots—Figs. 16c,f, which show the Z50 fields subtracted from the Z05 fields—reveal that the tangential winds inside the RMW of Z50 were stronger than for Z05. Additionally, the inflow at the surface was faster for Z05; however, the inflow and outflow layers were deeper for Z50. Thus, the results here are in agreement with the results from the simulations in Hlywiak and Nolan (2021).

Within the rear quadrants, increasing Z_0 enhanced the secondary circulation throughout the lower-troposphere except for at the RMW near the surface. Additionally, while tangential winds were weaker near the RMW for Z50 than for Z05, this relationship was reversed outside of the RMW. Specifically, stronger Z50 V_t was located around two RMW and $z = 2$ km. However, V_t outside of the RMW was stronger throughout the lower-troposphere for the smoother surface at landfall (not shown). Thus, a TC making landfall over a very rough surface may experience stronger winds inside the initial RMW, in addition to a deeper TCBL and land-forced acceleration of the low-level secondary circulation than for a TC making landfall over a smoother surface. Additionally, greater Z_0 enhanced the TCBL jet over the ocean up until landfall.

In summary, increasing the roughness contrast between the ocean and the inland surface amplified the responses documented in section 3. An inland roughness length of 50 cm led to a stronger inflow within the offshore flow and behind the TC than for a roughness length of 5 cm. Thus, TCBL winds to the rear and right of the Z50 TC were more supergradient than for Z05.

5. Case studies

Here, we analyze in situ and satellite data collected from three landfalling Gulf of Mexico hurricanes to find evidence in nature for increased inflow angles within the offshore flow before landfall. These hurricanes—Hurricanes Ike (2008), Harvey (2017), and Michael (2018)—were selected because they most closely resembled the TCs simulated for this research, i.e., they spent ample time over the Gulf of Mexico waters before making landfall at an angle fairly perpendicular to the coast. Additionally, two out of the three—Michael

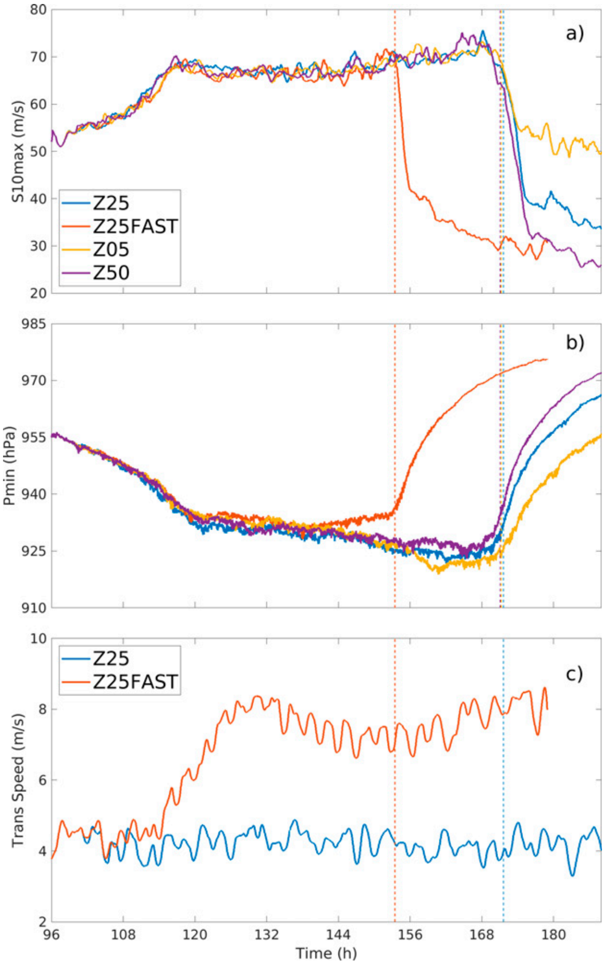

FIG. 12. (a) S10$_{max}$ (m s^{-1}), (b) P_{min} (hPa), and (c) translation speed (m s^{-1}) for Z25 (blue) and the three sensitivity simulations Z25FAST (red), Z05 (orange), and Z50 (purple) as a function of time. The respective vertical dashed lines mark the time of landfall for each TC. Note that Z25FAST reached the western edge of the domain earlier, thus ends around $t = 180$ h.

being the exception—occurred in late August or early September, transiting environments lacking significant vertical wind shear or midlatitude weather phenomena. The large-scale roughness of the Gulf Coast region is dominated by wetland environments toward the northwest and low forests toward the east. Thus, these TCs experienced conditions similar to the Z05 and Z25 simulations. We emphasize that this analysis is not meant to be comprehensive; rather, the goal here is to make a preliminary connection between the idealized simulations and reality.

Buoy and coastal station data were obtained from the National Data Buoy Center website. These stations provided basic meteorological data reported every six minutes when available. For this analysis, wind speed and direction were used to compute the inflow angles. The TC track data used to compute the radial and tangential winds comes from the revised Atlantic Hurricane Database HURDAT2 (Landsea and Franklin 2013), linearly interpolated to 6-min positions to match the buoy and station output frequency. Station locations were selected based on proximity to both storms, with an emphasis on stations between roughly 20 and 150 km from the landfall location. Equal numbers of stations to the left and right of landfall were desired; however, this was not always available. Additionally, station and buoy data were often incomplete, thus the following analysis only considers when stations reported data—i.e., no further interpolation of data was applied. The location of selected buoys and coastal stations relative to the track of each TC are shown in Fig. 17. Unfortunately, data were sparse and prone to failures mid-TC passage. For example, buoy 42043 was in an ideal location to observe the offshore inflow of Ike; however, this buoy went out of service well before landfall.

For Ike, surface wind data were obtained from the National Centers for Environmental Information's Blended Sea Winds dataset (Peng et al. 2013). This dataset covers the years 1987–2011, and thus was only available for Ike. This dataset blends several different satellite and in situ measurements to obtain as accurate an estimate of the surface winds as possible. Data are available at 6-h intervals. This gridded product is offered at a horizontal resolution of 0.25°, which is too coarse to observe the inner core winds associated with a TC but sufficient for observing trends in the broader wind field. (Note that the inflow angle values in Figs. 19c,f are extremely large for what is typically observed.) We suggest that the *exact* inflow angle values should be taken with some skepticism, as they are likely an artifact of the coarse resolution of the dataset. The overall changes in the inflow angle patterns appear to be valid, however.

a. Hurricane Ike

Hurricane Ike (2008) was a long-lived system that formed from an African easterly wave in late August (Berg 2009). After tracking across the Atlantic, the TC moved into the Gulf of Mexico where it regained category-2 intensity. Figures 18a–c shows the total and radial wind fields as well as inflow angles at the surface when the TC was located in the central part of the Gulf. At this time, Ike was embedded in an environment that lacked strong vertical wind shear or other disruptive environmental forces. The strongest total winds were located ahead of and within the front-right quadrants, while the strongest inflow was located within the rear-left quadrant.

Within the following two days, a subtropical ridge steered Ike toward the northwest, and the TC eventually made landfall perpendicular to the Texas coastline. Figures 18d–f show the wind field of Ike when the TC was located just offshore. At this time, the wind field over the ocean was much more symmetric, as strong winds were observed within both the onshore and the offshore flows. At the same time, the offshore flow was characterized by strong inflow and increased inflow angles. Thus, the evolution of Ike from this dataset resembled that of the idealized simulations presented here.

From the available data, Fig. 19 reveals the sustained winds and inflow angles experienced at each station during the passage of Ike. Until 13 September, it appears that the onshore

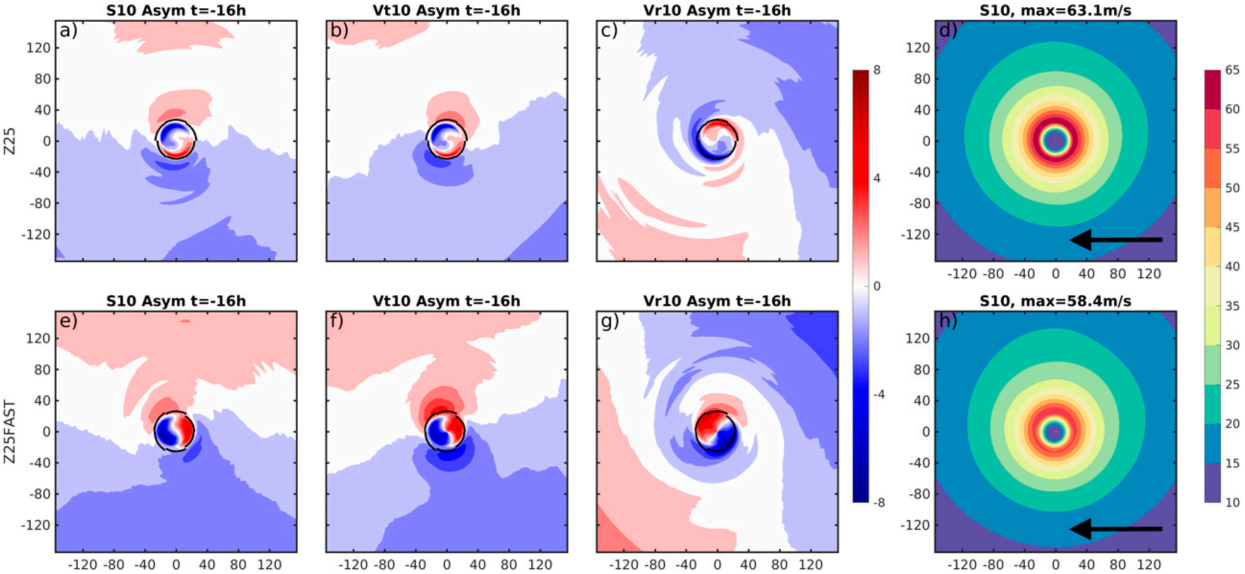

FIG. 13. As in Fig. 11, but for (a)–(d) Z25 and (e)–(h) Z25FAST at $t = -16$ h, when both TCs resided over the ocean.

stations—RLOT2 and SRST2—experienced slightly greater inflow angles on the order of 25° compared to near 0° for the offshore buoys. However, the available data were sparse.

For comparison with the idealized simulations, Fig. 20 shows plots of total wind speed and inflow angle for Z25 at six locations. Four of these were along the coast: OFF60L, OFF40L, ON40L, and ON60L. The other two were 25 km offshore over water: OFF40W and ON40W. These "stations" are located 60 and 40 km south of the landfall location within the offshore flow and 40 and 60 km north of the landfall location within the onshore flow. The greatest wind speeds between the six locations were generally observed onshore. The exception is with OFF40W, which observed winds that were several meters per second greater than for ON40W up until roughly 3 h before landfall.

Independent of wind speed, inflow angles increased in time up until landfall, reaching 45° offshore and 25° onshore. Most notably, inflow angles at OFF40W resembled the inflow angles for the onshore locations until 6 h before landfall. After this time, inflow angles at OFF40W increased dramatically to match the values observed at the coastal offshore locations. After landfall, inflow angles at all locations converged between 35° and 40°, as the rear TC quadrants were characterized by fairly uniform inflow angles.

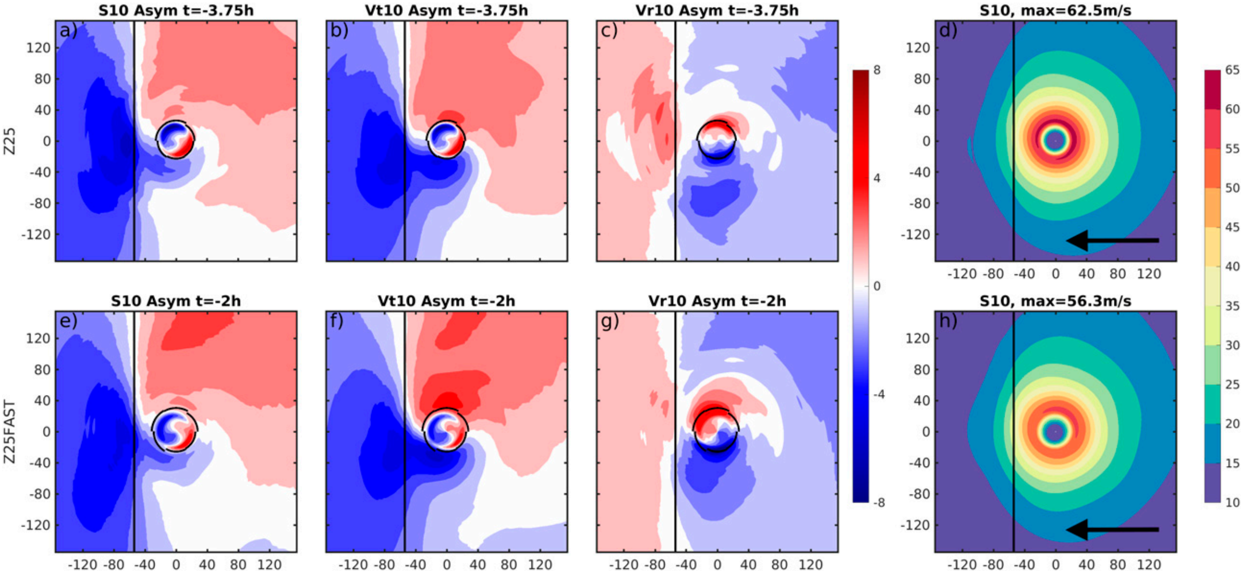

FIG. 14. As in Fig. 13, but at $t = -3.75$ for Z25 and $t = -2$ h for Z25FAST, when both TCs were roughly 50 km offshore.

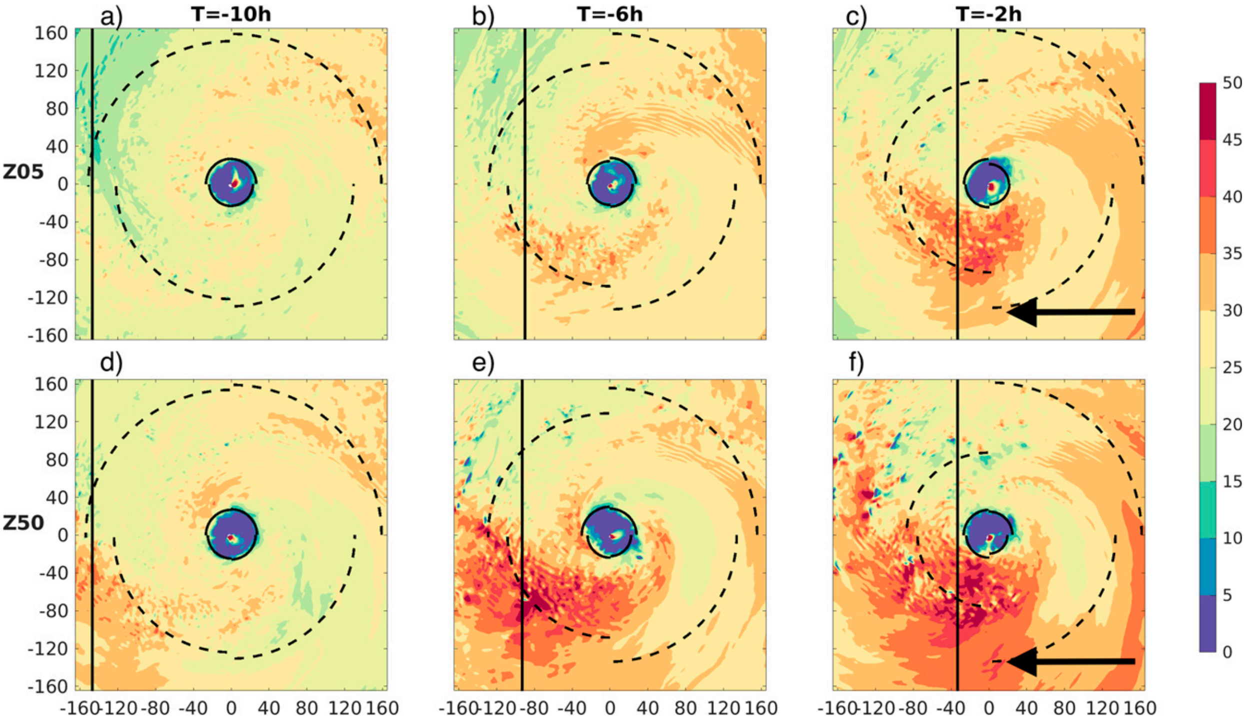

FIG. 15. Inflow angles (°) for (top) Z05 and (bottom) Z50 at t = (a),(d) −10; (b),(e) −6; and (c),(f) −10 h. Quadrant RMW and R18 are shown by the black solid and dashed lines, respectively. The location of land is marked by the vertical solid black line.

Inflow angle magnitudes from Ike and from Z25 were similar before landfall, and the observations show a continued increase after the passage of Ike. Unfortunately, partly due to a lack of consistent observations, a definitive statement regarding whether the observations from Ike support the results from the idealized experiments cannot be made.

b. Hurricane Harvey

Before infamously producing catastrophic rainfall over portions of eastern Texas and Louisiana, Hurricane Harvey (2018) made landfall along the Texas coast as a category-4 storm after traversing the western Gulf of Mexico (Blake and Zelinsky 2018). The following analysis focuses on this first landfall over Texas.

The location of the selected buoy and coastal stations for Harvey are shown in Figs. 17b and 21. The curvature of the Texas coastline prevented a purely perpendicular landfall, and it is likely that the presence of the coast to the west of Harvey influenced winds. Thus, stations along the perpendicular section of the coast are considered. Before landfall, the offshore stations—ANPT2 and MQTT2—reported inflow angles of roughly 40° and 65°, which remained consistent in time. Meanwhile, the onshore stations—MBET2 and AWRT2—experienced inflow angles of 0° and 35°. Between 1200 and 1800 UTC 25 August, the near-eyewall AWRT2 inflow angles were similar to that of the farther offshore MQTT2; however, after this time MQTT2 reported larger angles. Note that IRDT2 experienced a significant jump in inflow angles, from roughly 30° to greater than 100°. Because this station is located only 15 km from MQTT2, it is possible that IRDT2 was highly influenced by nearby inland obstacles.

Regardless, these offshore stations featured greater sustained inflow angles than the two onshore stations. Additionally, the values shown here were quite similar to those revealed in Figs. 5 and 20. Last, buoy (42020) experienced a significant increase in inflow angle in time, as with OFF40W in Fig. 20b. Thus, this case seems to support the evidence of elevated offshore inflow angles from section 3.

c. Hurricane Michael

Hurricane Michael (2018) rapidly intensified while over the eastern Gulf of Mexico and continued to intensify to a category-5 system up until landfall over the Florida Peninsula region (Beven II et al. 2019). Michael differs from the other two TCs in this section in that the storm formed late in the Atlantic hurricane season and interacted with an extratropical trough near land. Callaghan (2019) suggested that this interaction affected the thermal structure of the TC by facilitating warm-air advection to the west of the TC. Thus, the surface discontinuity was not the only factor altering the wind field leading up to landfall. Additionally, a cold-core eddy associated with the Loop Current system was in the vicinity of the TC (Wadler et al. 2021). These factors—in addition to possible rapid changes to the storm structure resulting from the rapid intensification—likely had an impact on the asymmetric wind structure.

The station and buoy locations are revealed in Figs. 17c and 22. Landfall occurred at 1730 UTC 10 October 2018. Data were

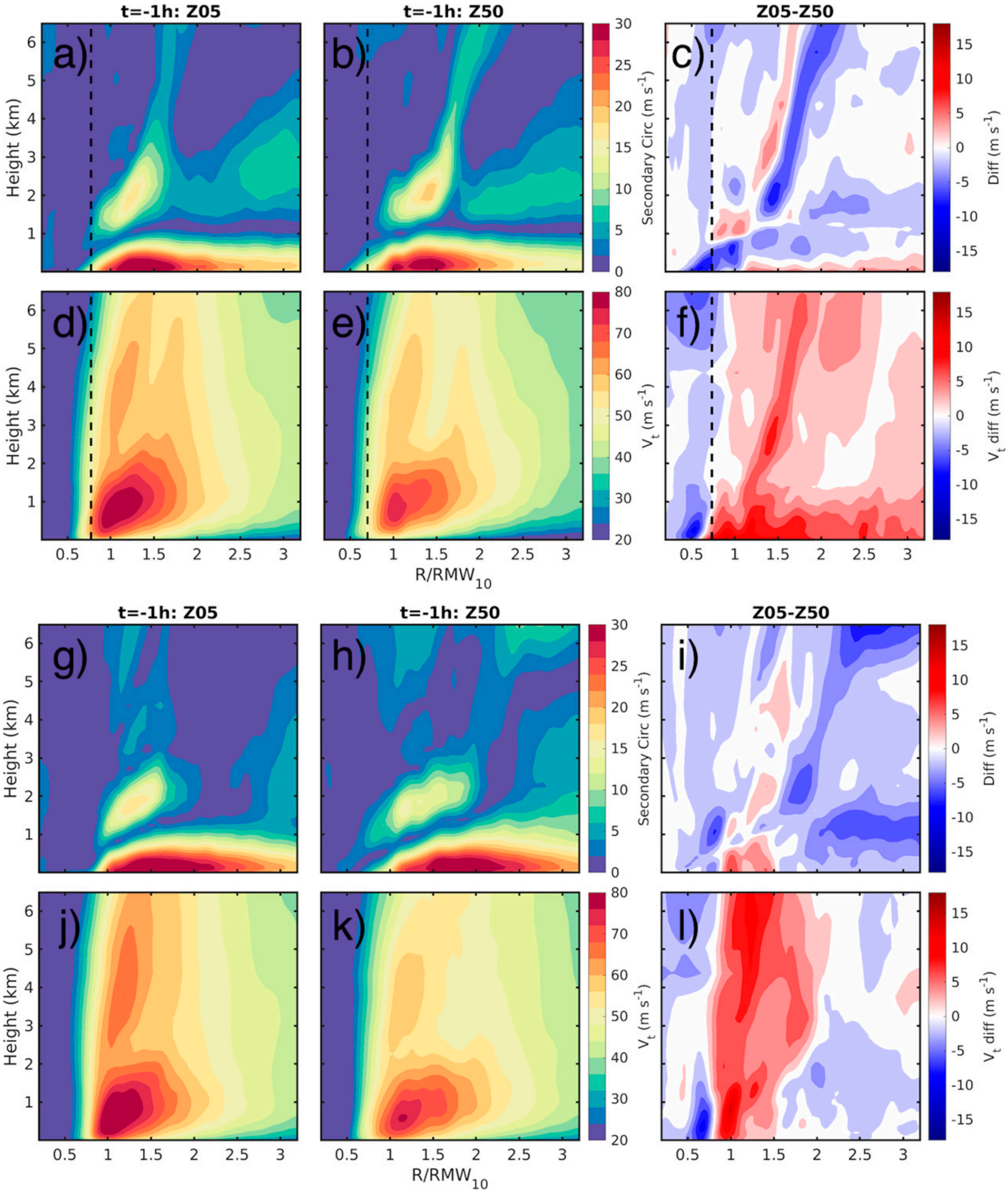

FIG. 16. (a)–(c),(g)–(i) Secondary circulation winds and (d)–(f),(j)–(l) V_t (m s^{-1}), azimuthally averaged over the front two quadrants in (a)–(f) and the rear two quadrants in (g)–(l) for Z05 and Z50 at landfall. The difference in each field is shown in (c), (f), (i), and (l), where red (blue) indicates stronger (weaker) winds for the Z05 winds. The radial coordinate is normalized by the instantaneous RMW for each TC. In (a)–(f), the coastline is marked by the vertical dashed line.

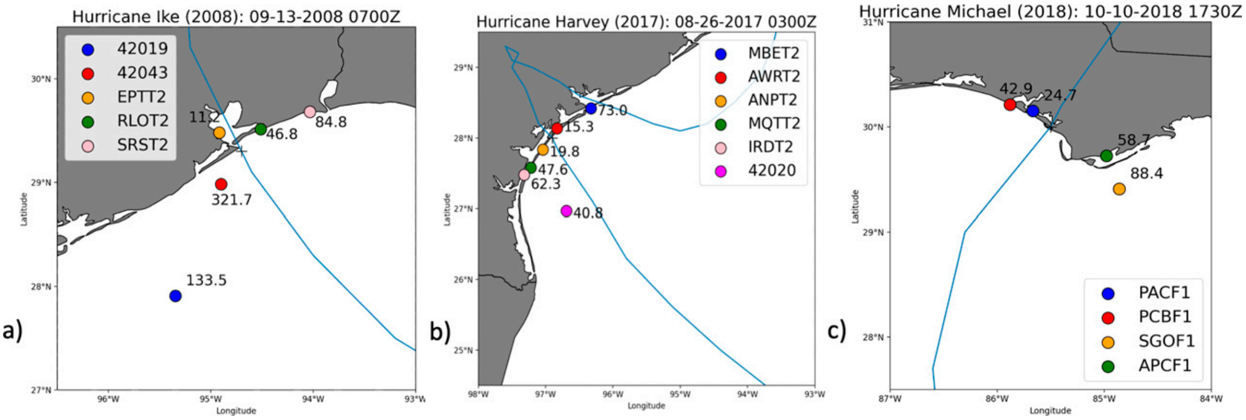

FIG. 17. Location of buoys and coastal stations along the Gulf of Mexico for Hurricanes (a) Ike, (b) Harvey, and (c) Michael. Tracks are shown by the blue plot, and the location and time of landfall are marked by the plus signs and the time within the title. The number next to each station indicates the minimum distance between the station and the track during the time period for which the station was active. For example, buoy 42043 went out of service when the center of Ike was 321.7 km away.

recorded uninterrupted from four stations—two offshore and two onshore—up until landfall. The coastal stations featured data that were highly periodic; however, from 0000 to 1700 UTC 10 October offshore inflow angles increased relative to the onshore angles by roughly 20°. These angles are also in agreement from those in Figs. 5 and 20. After landfall, the reporting three stations featured nearly identical inflow angles as all three stations became located to the rear of the TC. Thus, the evidence presented here seems to support the findings from section 3.

6. Summary and discussion

Here, idealized simulations of powerful TCs reveal that the TCBL wind field undergoes several modifications forced by the coastal discontinuity ahead of landfall. These modifications are simplified by the schematic in Fig. 23. Beginning 6–9 h before landfall, the outer portion of the wind field ahead of the TC rapidly decelerates near the surface over land due to increased friction. This forces high inflow angles over land while simultaneously weakening winds with distance inland.

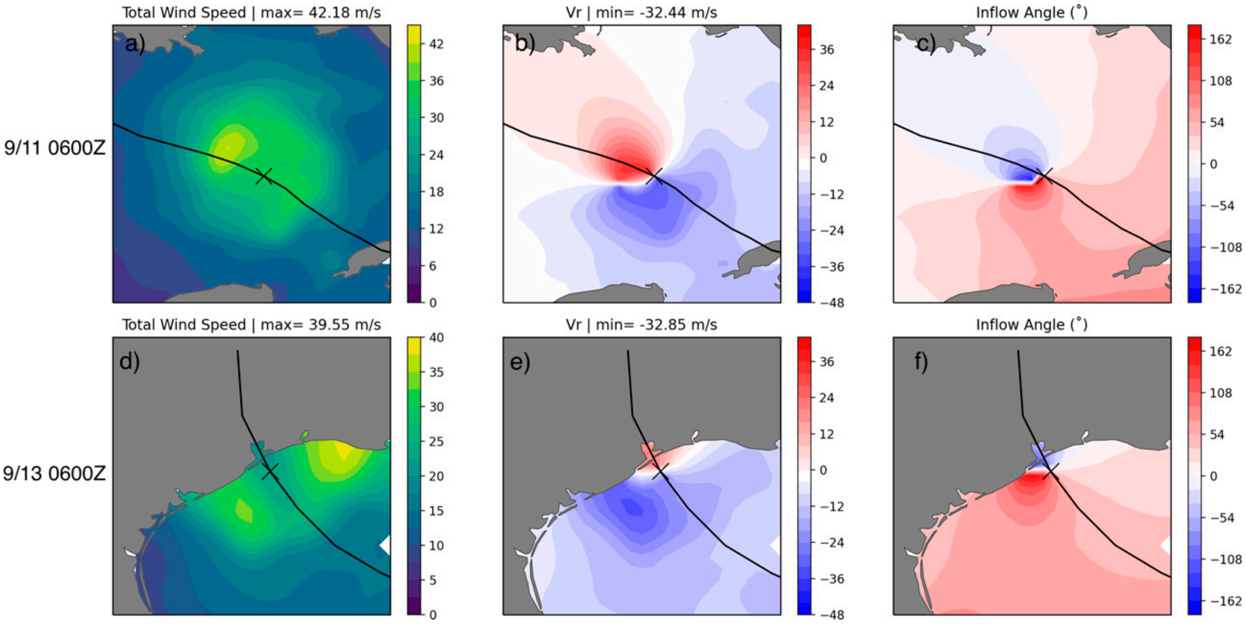

FIG. 18. (a),(d) Total wind speed (m s^{-1}); (b),(e) radial winds (m s^{-1}); and (c),(f) inflow angles (°) for Hurricane Ike at (top) 0600 UTC 11 Sep and (bottom) 0600 UTC 13 Sep. Wind data are taken from the NCEI Blended Winds Dataset (Peng et al. 2013). Track data, plotted by the solid black lines, is provided by HURDAT2. Note that due to the resolution of the wind field data, the wind field is not centered directly at the position of the TC.

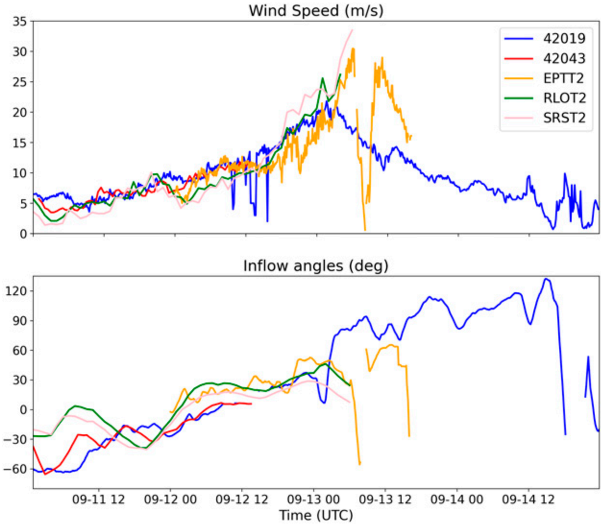

FIG. 19. Time series of (a) sustained wind speed and (b) inflow angle for each station during the landfall of Hurricane Ike. Gaps in the plots indicate missing data.

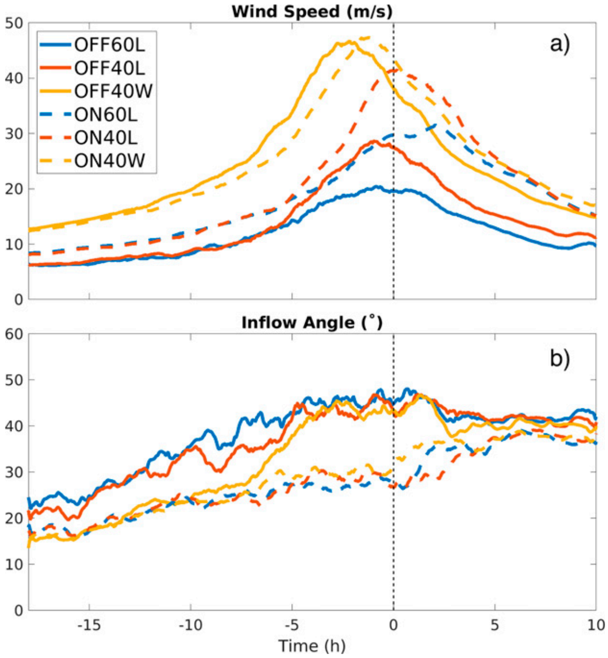

FIG. 20. Time series of (a) sustained wind speed and (b) inflow angle for six coastal locations within the Z25 simulation. Three "stations" are located within the offshore flow at 60 and 40 km south of the landfall location [solid plots; OFF60L (blue), OFF40L (red), and OFF40W (orange), respectively] and the other three are located at the equivalent distances north of the landfall location [dashed plots; ON60L (blue) and ON40L (red), and ON40W (orange), respectively]. The "L" indicates location at the coastline while the "W" indicates location 25 km offshore from the coastline over the water.

Once over the ocean, friction is dramatically reduced while the flow remains highly subgradient, resulting in an acceleration in the radial velocity. Thus, the advection of angular momentum by the secondary circulation downstream is enhanced. Convergence due to the inflow elevates vertical velocities near the TC core, adding to the inward advection of high momentum air by the secondary circulation. Thus, upper-TCBL winds to the rear and rear-right relative to the TC motion are enhanced before landfall. Alford et al. (2020) revealed that the supergradient TCBL jet may persist inland even as the near-surface flow deteriorates. The authors speculated that this could lead to stronger, more damaging gusts. Although not analyzed directly here, sporadic downdrafts may transport enhanced, supergradient flow toward the surface to the right of motion, leading to locally higher surface winds.

Sensitivity experiments revealed that increasing the surface roughness amplified these asymmetries. Additionally, a simulation with faster translation speed showed a similar evolution, indicating that the land-forced asymmetries are of a greater magnitude than the translation asymmetries. However, in the case of a landfall perpendicular to the coastline—these two effects may constructively interfere with each other to amplify the inflow response a few hours before landfall. In situ data from three landfalling hurricanes in nature provided evidence of elevated inflow angles within the offshore flow before landfall. A future analysis of observations of upper-TCBL winds before landfall would be beneficial to the arguments provided here.

The mechanism described here is similar to that presented by Shapiro (1983) and the similar Tang and Tan (2006). The coastal discontinuity in roughness appears to act similarly to the frictional gradient, yet at a much greater magnitude. Additionally, as the landmass was located directly ahead of the TC in our simulations, this pathway was rotated cyclonically by roughly 90° from that forced by the motion-induced friction asymmetry. Future trajectory analyses following air parcels around the TC before landfall would benefit this theory.

The simulated TCs here landfall at nearly perpendicular angles to the coast. Few landfalls in nature are this idyllic, and complex coastal geography is often involved. We hypothesize that changes to the landfall angle and shape of the coastline would rotate the region characterized by strong inflow angles. For example, a TC in the Gulf of Mexico translating toward the west roughly 100 miles south of the Gulf coastline may experience heightened inflow angles to the right of motion. Theoretically, the asymmetries forced by the coast would constructively interfere with inflow asymmetries forced by the TC motion, depending on the size of the TC and the distance offshore. However, continual advection of dry continental air from the north would deteriorate the tropical nature of the TC. Additionally, environmental vertical wind shear patterns often change drastically near land, which could force asymmetries near the surface that interact with the asymmetries forced by the presence of land. Thus, future research elucidating the wind response for angled landfalls would be greatly beneficial toward understanding the landfall process.

Investigations of internal boundary layer (IBL) development within the TCBL have accelerated within the past couple of decades (Hirth et al. 2012; Alford et al. 2020), as

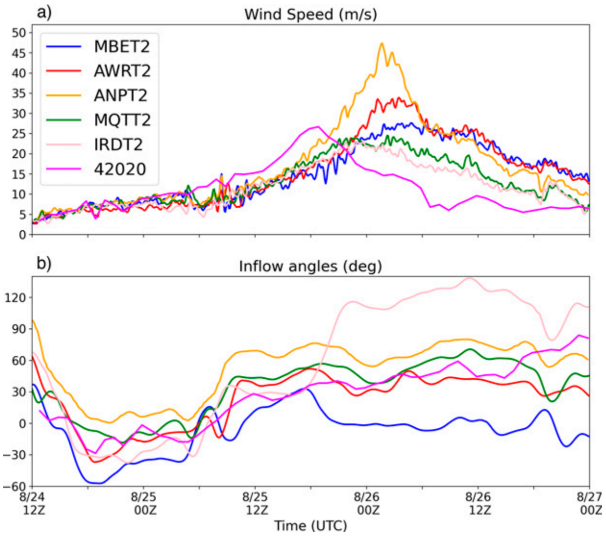

FIG. 21. Time series of (a) sustained wind speed and (b) inflow angle for each station during the initial landfall of Hurricane Harvey over Texas. Low-pass filters are applied to the observed data using minimum frequencies of 30 min in (a) and 3 h in (b).

improved wind sampling technologies within coastal regions have rendered such studies possible. Understanding the development of both onshore and offshore IBLs is a highly important problem, as these features modify local surface fluxes to an extent which may impact stress imparted on local infrastructure. Analyses of onshore IBL development within our simulations suggest that a logarithmic growth in the IBL height within a neutral boundary layer—see Hirth et al.'s (2012) Eq. (1)—is a valid approximation [refer to chapter 4 of Hlywiak (2021) for more information]. We refrain from discussing the IBL further here, as this was not a main focus of this manuscript. The exact near-surface wind structure and intensity of the surface fluxes here would be better simulated using large-eddy simulations embedded within a regional simulation framework.

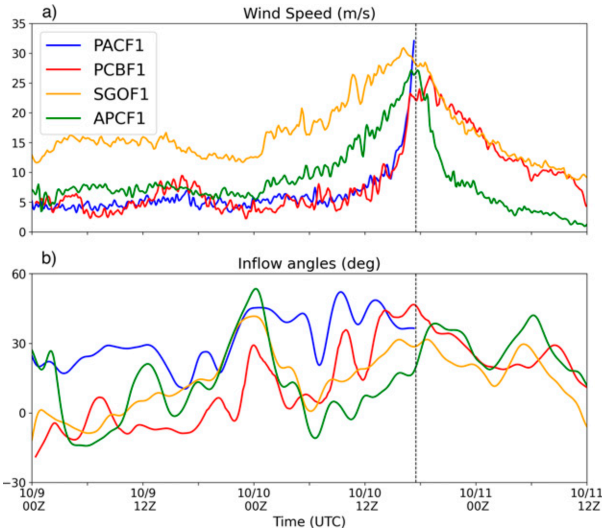

FIG. 22. As in Fig. 21, but for Hurricane Michael.

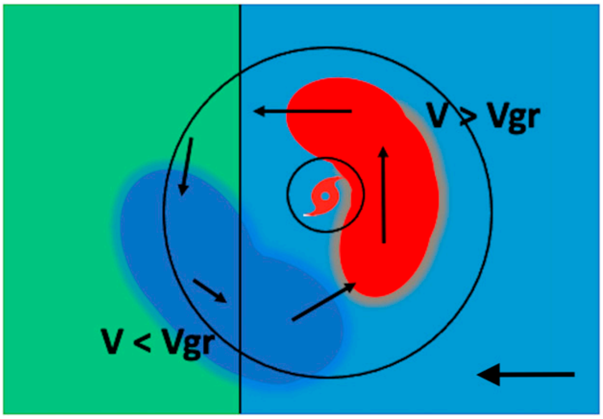

FIG. 23. Simple schematic illustrating the enhanced offshore inflow and acceleration of tangential winds behind the TC. The inner and outer wind fields are represented by small circle and larger oval, respectively, with the western portion over land. The oval is skewed toward the offshore side to represent the expansion of the tropical storm force wind area. Black arrows indicate the magnitude and direction of winds around the TC. The blue area represents the region of large inflow angles and subgradient winds, while the red area represents the supergradient winds at the top of the TCBL to the rear of the storm.

This pathway has profound implications for coastal hazard forecasting. A stronger upper-TCBL jet may possibly result in stronger gusts at the surface to due mixing of accelerated momentum above toward the surface. Thus, wind damages to the right-of-motion may be more severe than in situations where this structural evolution is absent. Additionally, many catastrophe and hazard models assume wind fields based on observations from over the ocean. For example, storm surge models rely on the surface wind speed and direction to compute wind stress and surge response. Thus, the results here imply that input wind fields should account for changes to the TCBL due to frictional convergence forced during landfall to improve accuracy.

Acknowledgments. J. Hlywiak was supported by a University of Miami Graduate Fellowship and both J. Hlywiak and D. Nolan were supported by NSF PREEVENTS Track 2 Award 1663947. We also thank Drs. Sharanya Majumdar, Lynn K. Shay, and George Bryan, and three anonymous reviewers for their valuable comments and advice toward improving this manuscript.

REFERENCES

Alford, A. A., M. I. Biggerstaff, G. D. Carrie, J. L. Schroeder, B. D. Hirth, and S. M. Waugh, 2019: Near-surface maximum winds during the landfall of Hurricane Harvey. *Geophys. Res. Lett.*, **46**, 973–982, https://doi.org/10.1029/2018GL080013.

——, J. A. Zhang, M. I. Biggerstaff, P. Dodge, F. D. Marks, and D. J. Bodine, 2020: Transition of the hurricane boundary layer during the landfall of Hurricane Irene (2011). *J. Atmos. Sci.*, **77**, 3509–3531, https://doi.org/10.1175/JAS-D-19-0290.1.

Bell, M. M., M. T. Montgomery, and K. A. Emanuel, 2012: Air–sea enthalpy and momentum exchange at major hurricane wind speeds observed during CBLAST. *J. Atmos. Sci.*, **69**, 3197–3222, https://doi.org/10.1175/JAS-D-11-0276.1.

Berg, R., 2009: Tropical cyclone report: Hurricane Ike (1–14 September 2008). National Hurricane Center Rep. AL092008, 55 pp., https://www.nhc.noaa.gov/data/tcr/AL092008_Ike.pdf.

Beven, J. L., II, R. Berg, and A. Hagen, 2019: Tropical cyclone report: Hurricane Michael (7–11 October 2018). National Hurricane Center Rep. AL142018, 86 pp., https://www.nhc.noaa.gov/data/tcr/AL142018_Michael.pdf.

Blackwell, K. G., 2000: The evolution of Hurricane Danny (1997) at landfall: Doppler-observed eyewall replacement, vortex contraction/intensification, and low-level wind maxima. *Mon. Wea. Rev.*, **128**, 4002–4016, https://doi.org/10.1175/1520-0493(2000)129<4002:TEOHDA>2.0.CO;2.

Blake, E. S., and D. A. Zelinsky, 2018: Tropical cyclone report: Hurricane Harvey (17 August–1 September 2017). National Hurricane Center Rep. AL092017, 77 pp., https://www.nhc.noaa.gov/data/tcr/AL092017_Harvey.pdf.

Callaghan, J., 2019: The interaction of Hurricane Michael with an upper trough leading to intensification right up to landfall. *Trop. Cyclone Res. Rev.*, **8**, 95–102, https://doi.org/10.1016/j.tcrr.2019.07.009.

Cao, Y., and R. G. Fovell, 2016: Downslope windstorms of San Diego County. Part I: A case study. *Mon. Wea. Rev.*, **144**, 529–552, https://doi.org/10.1175/MWR-D-15-0147.1.

Chen, F., and J. Dudhia, 2001: Coupling an advanced land surface–hydrology model with the Penn State–NCAR MM5 modeling system. Part I: Model implementation and sensitivity. *Mon. Wea. Rev.*, **129**, 569–585, https://doi.org/10.1175/1520-0493(2001)129<0569:CAALSH>2.0.CO;2.

Chen, Y., and M. K. Yau, 2003: Asymmetric structures in a simulated landfalling hurricane. *J. Atmos. Sci.*, **60**, 2294–2312, https://doi.org/10.1175/1520-0469(2003)060<2294:ASIASL>2.0.CO;2.

Donelan, M. A., B. K. Haus, N. Reul, W. J. Plant, M. Stiassnie, H. C. Graber, O. B. Brown, and E. S. Saltzman, 2004: On the limiting aerodynamic roughness of the ocean in very strong winds. *Geophys. Res. Lett.*, **31**, L18306, https://doi.org/10.1029/2004GL019460.

Edson, J. B., and Coauthors, 2013: On the exchange of momentum over the open ocean. *J. Phys. Oceanogr.*, **43**, 1589–1610, https://doi.org/10.1175/JPO-D-12-0173.1.

Green, B. W., and F. Zhang, 2013: Impacts of air–sea flux parameterizations on the intensity and structure of tropical cyclones. *Mon. Wea. Rev.*, **141**, 2308–2324, https://doi.org/10.1175/MWR-D-12-00274.1.

Hirth, B. D., J. L. Schroeder, C. C. Weiss, D. A. Smith, and M. I. Biggerstaff, 2012: Research radar analyses of the internal boundary layer over Cape Canaveral, Florida, during the landfall of Hurricane Frances (2004). *Wea. Forecasting*, **27**, 1349–1372, https://doi.org/10.1175/WAF-D-12-00014.1.

Hlywiak, J., 2021: Modifications to the tropical cyclone intensity and wind structure resulting from surface-boundary layer interactions over coastal and inland environments. Ph.D. thesis, University of Miami, 206 pp.

——, and D. S. Nolan, 2021: The response of the near-surface tropical cyclone wind field to inland surface roughness length and soil moisture content during and after landfall. *J. Atmos. Sci.*, **78**, 983–1000, https://doi.org/10.1175/JAS-D-20-0211.1.

Hong, S. Y., Y. Noh, and J. Dudhia, 2006: A new vertical diffusion package with an explicit treatment of entrainment processes. *Mon. Wea. Rev.*, **134**, 2318–2341, https://doi.org/10.1175/MWR3199.1.

Janjić, Z. I., 2002: Nonsingular implementation of the Mellor–Yamada Level 2.5 scheme in the NCEP Meso model. NCEP Office Note 437, 61 pp., http://www.emc.ncep.noaa.gov/officenotes/newernotes/on437.pdf.

Jordan, C. L., 1958: Mean soundings for the West Indies area. *J. Meteor.*, **15**, 91–97, https://doi.org/10.1175/1520-0469(1958)015<0091:MSFTWI>2.0.CO;2.

Kepert, J., 2006: Observed boundary layer wind structure and balance in the hurricane core. Part II: Hurricane Mitch. *J. Atmos. Sci.*, **63**, 2169–2193, https://doi.org/10.1175/JAS3745.1.

——, and Y. Wang, 2001: The dynamics of boundary layer jets within the tropical cyclone core. Part II: Nonlinear enhancement. *J. Atmos. Sci.*, **58**, 2485–2501, https://doi.org/10.1175/1520-0469(2001)058<2485:TDOBLJ>2.0.CO;2.

Klotz, B. W., and H. Jiang, 2017: Examination of surface wind asymmetries in tropical cyclones. Part I: General structure and wind shear impacts. *Mon. Wea. Rev.*, **145**, 3989–4009, https://doi.org/10.1175/MWR-D-17-0019.1.

Knaff, J. A., S. P. Longmore, R. T. DeMaria, and D. A. Molenar, 2015: Improved tropical-cyclone flight-level wind estimates using routine infrared satellite reconnaissance. *J. Appl. Meteor. Climatol.*, **54**, 463–478, https://doi.org/10.1175/JAMC-D-14-0112.1.

Landsea, C. W., and J. L. Franklin, 2013: Atlantic hurricane database uncertainty and presentation of a new database format. *Mon. Wea. Rev.*, **141**, 3576–3592, https://doi.org/10.1175/MWR-D-12-00254.1.

Li, X., Z. Pu, and Z. Gao, 2021: Effects of roll vortices on the evolution of Hurricane Harvey during landfall. *J. Atmos. Sci.*, **78**, 1847–1867, https://doi.org/10.1175/JAS-D-20-0270.1.

Li, Y., K. K. Cheung, and J. C. Chan, 2014: Numerical study on the development of asymmetric convection and vertical wind shear during tropical cyclone landfall. *Quart. J. Roy. Meteor. Soc.*, **140**, 1866–1877, https://doi.org/10.1002/qj.2259.

——, ——, and J. C. Chan, 2015: Modelling the effects of land-sea contrast on tropical cyclone precipitation under environmental vertical wind shear. *Quart. J. Roy. Meteor. Soc.*, **141**, 396–412, https://doi.org/10.1002/qj.2359.

Lim, J. O. J., and S. Y. Hong, 2005: Effects of bulk ice microphysics on the simulated monsoonal precipitation over East Asia. *J. Geophys. Res.*, **110**, D2420, https://doi.org/10.1029/2005JD006166.

Morrison, I., S. Businger, F. Marks, P. Dodge, and J. A. Businger, 2005: An observational case for the prevalence of roll vortices in the hurricane boundary layer. *J. Atmos. Sci.*, **62**, 2662–2673, https://doi.org/10.1175/JAS3508.1.

Nolan, D. S., 2011: Evaluating environmental favorableness for tropical cyclone development with the method of point-downscaling. *J. Adv. Model. Earth Syst.*, **3**, M08001, https://doi.org/10.1029/2011MS000063.

——, D. P. Stern, and J. A. Zhang, 2009a: Evaluation of planetary boundary layer parameterizations in tropical cyclones by comparison of in situ observations and high-resolution simulations of Hurricane Isabel (2003). Part II: Inner-core boundary layer and eyewall structure. *Mon. Wea. Rev.*, **137**, 3675–3698, https://doi.org/10.1175/2009MWR2786.1.

——, J. A. Zhang, and D. P. Stern, 2009b: Evaluation of planetary boundary layer parameterizations in tropical cyclones by comparison of in situ observations and high-resolution simulations of Hurricane Isabel (2003). Part I: Initialization, maximum winds, and the outer-core boundary layer. *Mon. Wea. Rev.*, **137**, 3651–3674, https://doi.org/10.1175/2009MWR2785.1.

——, B. D. McNoldy, and J. Yunge, 2021a: Evaluation of the surface wind field over land in WRF simulations of Hurricane Wilma (2005). Part I: Model initialization and simulation validation. *Mon. Wea. Rev.*, **149**, 679–695, https://doi.org/10.1175/MWR-D-20-0199.1.

——, ——, J. Yunge, F. J. Masters, and I. M. Giammanco, 2021b: Evaluation of the surface wind field over land in WRF simulations of Hurricane Wilma (2005). Part II: Surface winds, inflow angles, and boundary layer profiles. *Mon. Wea. Rev.*, **149**, 697–713, https://doi.org/10.1175/MWR-D-20-0201.1.

Onderlinde, M. J., and D. S. Nolan, 2017: The tropical cyclone response to changing wind shear using the method of time-varying point-downscaling. *J. Adv. Model. Earth Syst.*, **9**, 908–931, https://doi.org/10.1002/2016MS000796.

Peng, G., H. M. Zhang, H. P. Frank, J. R. Bidlot, M. Higaki, S. Stevens, and W. R. Hankins, 2013: Evaluation of various surface wind products with ocean SITES buoy measurements. *Wea. Forecasting*, **28**, 1281–1303, https://doi.org/10.1175/WAF-D-12-00086.1.

Powell, M. D., 1982: The transition of the Hurricane Frederic boundary-layer wind field from the open Gulf of Mexico to landfall. *Mon. Wea. Rev.*, **110**, 1912–1932, https://doi.org/10.1175/1520-0493(1982)110<1912:TTOTHF>2.0.CO;2.

——, S. H. Houston, L. R. Amat, and N. Morisseau-Leroy, 1998: The HRD real-time hurricane wind analysis system. *J. Wind Eng. Ind. Aerodyn.*, **77–78**, 53–64, https://doi.org/10.1016/S0167-6105(98)00131-7.

Shapiro, L. J., 1983: The asymmetric boundary layer flow under a translating hurricane. *J. Atmos. Sci.*, **40**, 1984–1998, https://doi.org/10.1175/1520-0469(1983)040<1984:TABLFU>2.0.CO;2.

Szeto, K. C., and J. C. Chan, 2010: Structural changes of a tropical cyclone during landfall: β-plane simulations. *Adv. Atmos. Sci.*, **27**, 1143–1150, https://doi.org/10.1007/s00376-009-9136-x.

Tang, X., and Z. Tan, 2006: Boundary-layer wind structure in a landfalling tropical cyclone. *Adv. Atmos. Sci.*, **23**, 737–749, https://doi.org/10.1007/s00376-006-0737-3.

Uhlhorn, E. W., B. W. Klotz, T. Vukicevic, P. D. Reasor, and R. F. Rogers, 2014: Observed hurricane wind speed asymmetries and relationships to motion and environmental shear. *Mon. Wea. Rev.*, **142**, 1290–1311, https://doi.org/10.1175/MWR-D-13-00249.1.

Wadler, J. B., J. A. Zhang, R. F. Rogers, B. Jaimes, and L. K. Shay, 2021: The rapid intensification of Hurricane Michael (2018): Storm structure and the relationship to environmental and air–sea interactions. *Mon. Wea. Rev.*, **149**, 245–267, https://doi.org/10.1175/MWR-D-20-0145.1.

Williams, G. J., 2019: Idealized simulations of the inner core boundary layer structure in a landfalling tropical cyclone. Part I: Kinematic structure. *Trop. Cyclone Res. Rev.*, **8**, 47–67, https://doi.org/10.1016/j.tcrr.2019.07.006.

Wong, M. L., and J. C. Chan, 2007: Modeling the effects of land-sea roughness contrast on tropical cyclone winds. *J. Atmos. Sci.*, **64**, 3249–3264, https://doi.org/10.1175/JAS4027.1.

Xu, W., H. Jiang, and X. Kang, 2014: Rainfall asymmetries of tropical cyclones prior to, during, and after making landfall in South China and Southeast United States. *Atmos. Res.*, **139**, 18–26, https://doi.org/10.1016/j.atmosres.2013.12.015.

Zhang, C., Y. Wang, and K. Hamilton, 2011: Improved representation of boundary layer clouds over the southeast Pacific in ARW-WRF using a modified Tiedtke cumulus parameterization scheme. *Mon. Wea. Rev.*, **139**, 3489–3513, https://doi.org/10.1175/MWR-D-10-05091.1.

Zhang, J. A., and E. W. Uhlhorn, 2012: Hurricane sea surface inflow angle and an observation-based parametric model. *Mon. Wea. Rev.*, **140**, 3587–3605, https://doi.org/10.1175/MWR-D-11-00339.1.

——, R. F. Rogers, D. S. Nolan, and F. D. Marks, 2011a: On the characteristic height scales of the hurricane boundary layer. *Mon. Wea. Rev.*, **139**, 2523–2535, https://doi.org/10.1175/MWR-D-10-05017.1.

——, P. Zhu, F. J. Masters, R. F. Rogers, and F. D. Marks, 2011b: On momentum transport and dissipative heating during hurricane landfalls. *J. Atmos. Sci.*, **68**, 1397–1404, https://doi.org/10.1175/JAS-D-10-05018.1.

——, R. F. Rogers, P. D. Reasor, E. W. Uhlhorn, and F. D. Marks, 2013: Asymmetric hurricane boundary layer structure from dropsonde composites in relation to the environmental vertical wind shear. *Mon. Wea. Rev.*, **141**, 3968–3984, https://doi.org/10.1175/MWR-D-12-00335.1.